POLITECNICO DI TORINO
Repository ISTITUZIONALE

Core integrated simulations for the Divertor Tokamak Test facility scenarios towards consistent core-pedestal-SOL modelling

Original
Core integrated simulations for the Divertor Tokamak Test facility scenarios towards consistent core-pedestal-SOL modelling / Casiraghi, I; Mantica, P; Ambrosino, R; Aucone, L; Baiocchi, B; Balbinot, L; Barberis, T; Castaldo, A; Cavedon, M; Frassinetti, L; Innocente, P; Koechl, F; Nowak, S; Agostinetti, P; Ceccuzzi, S; Figini, L; Granucci, G; Vincenzi, P. - In: PLASMA PHYSICS AND CONTROLLED FUSION. - ISSN 0741-3335. - 65:3(2023), p. 035017. [10.1088/1361-6587/acb6b1]

Availability:
This version is available at: 11583/2976849 since: 2023-03-13T10:53:31Z

Publisher:
IOP Publishing

Published
DOI:10.1088/1361-6587/acb6b1

Terms of use:
openAccess

This article is made available under terms and conditions as specified in the corresponding bibliographic description in the repository

Publisher copyright

(Article begins on next page)

29 March 2023

Plasma Physics and Controlled Fusion

PAPER • OPEN ACCESS

Core integrated simulations for the Divertor Tokamak Test facility scenarios towards consistent core-pedestal-SOL modelling

To cite this article: I Casiraghi *et al* 2023 *Plasma Phys. Control. Fusion* **65** 035017

View the article online for updates and enhancements.

You may also like

- Small molecule donors with different conjugated linking bridges: Synthesis and photovoltaic properties
Xiyue Dong, Dingqin Hu, Pengyu Chen et al.
- Poly(3,5-dithiophene-2-yldithieno[3,2-b;2,3-d]thiophene-co-Ethylenedioxythiophene)/Glassy Carbon Electrode Formation and Electrochemical Impedance Spectroscopic Study
Murat Ates, Ipek Osken and Turan Ozturk
- DTT: a divertor tokamak test facility for the study of the power exhaust issues in view of DEMO
R. Albanese, on behalf of the WPDTT2 Team and the DTT Project Proposal Contributors

This content was downloaded from IP address 194.81.223.66 on 13/03/2023 at 10:44

OPEN ACCESS
IOP Publishing
Plasma Physics and Controlled Fusion
Plasma Phys. Control. Fusion **65** (2023) 035017 (18pp)
https://doi.org/10.1088/1361-6587/acb6b1

Core integrated simulations for the Divertor Tokamak Test facility scenarios towards consistent core-pedestal-SOL modelling

I Casiraghi[2,3,*], P Mantica[3], R Ambrosino[1,4,5], L Aucone[2,3], B Baiocchi[3], L Balbinot[6], T Barberis[7], A Castaldo[8], M Cavedon[2], L Frassinetti[9], P Innocente[10,11], F Koechl[12], S Nowak[3], P Agostinetti[10,11], S Ceccuzzi[1,8], L Figini[3], G Granucci[3] and P Vincenzi[10,11]

[1] DTT S.C. a r.l., Frascati, Italy
[2] Dipartimento di Fisica 'G. Occhialini', Universitá di Milano-Bicocca, Milano, Italy
[3] Istituto per la Scienza e Tecnologia dei Plasmi, CNR, Milano, Italy
[4] Universitá degli Studi di Napoli Federico II, Napoli, Italy
[5] Consorzio CREATE, Napoli, Italy
[6] Dipartimento di Economia, Ingegneria, Societá e Impresa, Universitá della Tuscia, Viterbo, Italy
[7] DISAT, Politecnico di Torino, Torino, Italy
[8] ENEA C.R.Frascati, Frascati, Italy
[9] Fusion Plasma Physics, ECSS, KTH Royal Institute of Technology, Stockholm, Sweden
[10] Consorzio RFX (CNR, ENEA, INFN, UNIPD, Acciaierie Venete SpA), Padova, Italy
[11] Istituto per la Scienza e Tecnologia dei Plasmi, CNR, Padova, Italy
[12] CCFE, Culham Science Centre, Abingdon, United Kingdom

E-mail: irene.casiraghi@istp.cnr.it

Received 7 October 2022, revised 10 January 2023
Accepted for publication 27 January 2023
Published 10 February 2023

Abstract

Deuterium plasma discharges of the Divertor Tokamak Test facility (DTT) in different operational scenarios have been predicted by a comprehensive first-principle based integrated modelling activity using state-of-art quasi-linear transport models. The results of this work refer to the updated DTT configuration, which includes a device size optimisation (enlargement to $R_0 = 2.19$ m and $a = 0.70$ m) and upgrades in the heating systems. The focus of this paper is on the core modelling, but special attention was paid to the consistency with the scrape-off layer parameters required to achieve divertor plasma detachment. The compatibility of these physics-based predicted scenarios with the electromagnetic coil system capabilities was then verified. In addition, first estimates of DTT sawteeth and of DTT edge localised modes were achieved.

* Author to whom any correspondence should be addressed.

Original Content from this work may be used under the terms of the Creative Commons Attribution 4.0 licence. Any further distribution of this work must maintain attribution to the author(s) and the title of the work, journal citation and DOI.

Keywords: integrated modelling, Divertor Tokamak Test facility, DTT, turbulent transport, core-edge-SOL simulations

(Some figures may appear in colour only in the online journal)

1. Introduction

To align the research priorities towards the electricity production from thermonuclear fusion energy, a list of eight challenges to be faced was defined in the European fusion roadmap [1, 2]. Finding a reliable solution for the problem of the controlled exhaust of energy and particles from a fusion reactor is the second mission goal. All plasma-facing components must withstand the large particle and heat fluxes of a fusion reactor (up to 10–20 MW m^{-2}). The baseline strategy of employing a conventional metal divertor in single null (SN) configuration operating in partially detached plasma conditions, adopted in ITER [3], could not be directly extrapolated to DEMO [4] and future commercial fusion power plants, so alternative strategies need to be explored. In this framework, a new tokamak facility dedicated to study power exhaust is under construction in Italy: the Divertor Tokamak Test facility (DTT) [5, 6].

The DTT machine is a D-shaped superconducting tokamak, under construction at the ENEA Research Center in Frascati, whose parameters have been optimised to be as similar as possible with the operating conditions in DEMO. A detailed description of the DTT project is reported in [7], where the main parameters of DTT are compared to those of ITER and EU DEMO.

In DTT ($R_0 = 2.19$ m, $a = 0.70$ m, tungsten first wall (FW) and divertor, superconducting coils, pulse length $\leqslant 100$ s, clockwise vacuum toroidal field from above $B_{\rm tor} \leqslant 5.85$ T, counter-clockwise plasma current from above $|I_{\rm pl}| \leqslant 5.5$ MA, equipped with electron cyclotron resonance heating (ECRH), neutral beam injector (NBI), and ion cyclotron resonance heating (ICRH) systems for a total auxiliary heating $\leqslant$ 45 MW) different divertor solutions and improved plasma-facing materials will be developed and tested, including advanced magnetic configurations (such as double null, quasi-snowflake, and SN with negative triangularity scenarios) and liquid metal divertors.

In order to minimise risks and reduce costs, a first-principle based integrated modelling as comprehensive as possible of plasma discharges in different operational scenarios is a fundamental tool for designing a new tokamak. Therefore, main DTT scenarios were simulated for the initial machine configuration with $R_0 = 2.14$ m, as reported in [7]. This work led to the optimisation of the device size, increased to $R_0 =$ 2.19 m, and of the reference heating mix, as widely described in [7].

After this initial work, it became evident that the core simulations needed to be consistent with the requirements to achieve divertor plasma conditions compatible with current technologies. Particularly, scrape-off layer (SOL) and divertor plasma simulations [8] performed with the 2D edge numerical code SOLEDGE2D-EIRENE [9, 10] estimated the minimum separatrix density and impurity concentration required to obtain sustainable conditions in full power operations. Therefore a new thread of simulations was started for the machine configuration $R_0 = 2.19$ m, in which particular attention was paid to the integration of the core and pedestal runs with the SOL modelling.

In this paper, the latest results for the new machine configuration with $R_0 = 2.19$ m of the multi-channel core integrated simulations based on state-of-art first-principle quasi-linear (QL) transport models of the DTT baseline scenarios are presented. The modelling is now updated to the current DTT configuration, including the machine enlargement and the consequent auxiliary heating system upgrades. This work provides reference profiles for diagnostic system design, estimates of neutron yields, calculations of fast particle losses, fuelling requirements, magnetohydrodynamics (MHD) evaluations, and other tasks.

Great efforts have been made to obtain plasma scenarios compatible with divertor and FW power handling capability and tungsten influx. To avoid the tungsten melting, the heat loads should be lower than 20 MW m^{-2} to the divertor, 7.5 MW m^{-2} to the internal FW, and 1 MW m^{-2} to the external wall [11]. To avoid the erosion and the consequent high tungsten influx and core accumulation, the plasma temperature should not exceed the value of 5 eV at both the divertor and the wall [11]. Therefore, DTT should operate with plasma in partially and fully detached states with the latter that could be more relevant for DEMO. The SOL modelling indicates that the detachment conditions require a strong radiation by impurity seeding and high separatrix density values, which at the end affects pedestal properties [12]. These requirements have been taken into account in the core and pedestal simulations by setting suitable values at the separatrix as boundary conditions. Different seeding gases have also been tested.

The consistency between the control coil system capabilities and plasma profiles has been checked too.

In addition, an analysis of sawteeth in DTT using the Porcelli model [13] has been carried out for the first time and some considerations on the possible impact of edge localised modes (ELMs) have been made based on existing scalings [14–17].

2. The DTT integrated modelling

An extensive modelling work of DTT scenarios has been conducted for the last 3 years. The baseline scenarios with the SN configuration with positive triangularity in H-mode during the flat-top phase are now available for the new DTT design. These core integrated simulations predict radial profiles of the electron and ion temperatures, density (both main species and impurity), toroidal rotation, and current density, calculating consistently the magnetic equilibrium, the heating profiles,

Table 1. DTT scenarios with the SN configuration.

Phase	$\lvert I_{pl}\rvert$ (MA)	Vacuum B_{tor} (T)	ECRH installed power (MW)	ICRH installed power (MW)	NBI installed power (MW)
A1	2.0	3.0	8.0	0.0	0.0
B1	2.0	3.0	16.0	4.0	0.0
C1	4.0	5.85	16.0	4.0	0.0
D1	5.5	5.85	16.0	4.0	10.0
E1	5.5	5.85	32.0	8.0	10.0

and the non-linear interactions between the different transport channels and between heating and plasma. The core runs cover the region from the plasma centre up to the separatrix.

With respect to the configurations previously studied in [7], the latest changes of the baseline scenarios are included in this paper. To this day, the planned DTT scenarios with the SN magnetic configuration are called A1, B1, C1, D1, and E1. These reference scenarios are characterised by the values of plasma current, toroidal magnetic field, and auxiliary heating system powers listed in table 1. The scenarios A1–B1–C1 are foreseen in the period 2028–2032, whilst D1 and E1 from 2032 onwards.

To enhance the reliability of our modelling predictions, matching as well as possible the key parameters between core and SOL simulations is an essential aspect. Firstly, an investigation work about the SOL parameter ranges in existing tokamaks (C-mod and JET), described in [18], was done to establish the best set of input parameters for DTT.

Several SOL simulations, whose details are also reported in [12], were performed with the SOLEDGE2D-EIRENE code in order to define the detachment conditions in the main DTT baseline scenarios: the A1 scenario (the first plasma scenario), the C1 scenario (the half power scenario), and the E1 scenario (the full power scenario with positive triangularity).

The SOLEDGE2D-EIRENE simulations, coupling a fluid kinetic code for plasma with the neutral dynamics, cover the region from $\rho_{tor} = 0.85$ (just inside the pedestal top) up to the entire FW, where the normalised effective minor radius $\rho_{tor} := \sqrt{(\Phi/\pi B_{tor})/(\Phi/\pi B_{tor})_{sep}}$ is the normalised radius that a magnetic surface with circular section should have to enclose the same toroidal magnetic flux Φ. A detailed description of the SOL modelling is out of scope of this paper and is presented in [12]. In the rest of this paper, the expression 'SOL modelling' refers to these SOLEDGE2D–EIRENE simulations from $\rho_{tor} = 0.85$ to the FW.

Then, we proceeded iteratively with a work of adjustment of the simulation settings, operating on both sides (core and SOL modelling). Particularly, the SOL modelling takes as input from the core modelling the values of power flowing outward from the separatrix and its splitting between the electron and the ion channels, while in the core modelling the impurity contents and the plasma pressure boundary conditions are set based on separatrix values calculated by the SOL modelling. Moreover, the core modelling transport profiles were used in [18] to better tune specific DTT transport coefficients to be used in the SOL modelling of DTT scenarios [12].

Summarising, the results of the DTT SOL modelling entails strenuous requirements in the core simulations discussed in this paper in terms of impurity concentrations and pedestal parameters to reach detachment conditions, as specified in the following sections for each analysed scenario.

2.1. General settings of core simulations

This paper concerns the integrated modelling of DTT scenarios with the SN configuration with positive triangularity. The core simulations of DTT deuterium plasmas during the flat-top phases were mainly performed using the JINTRAC [19] modelling suite with its core plasma transport code JETTO [20], and in some cases employing the transport solver ASTRA [21, 22] within a mixed iterative ASTRA–JINTRAC approach thoroughly discussed in [7].

Although these runs cover the region inside the separatrix (with a grid of 100 equally spaced radial points from the plasma centre up to the separatrix), the transport equations for heat, particle, and momentum are solved only within the top of the pedestal.

The neoclassical heat and particle transport is calculated by the NCLASS [23] model, while the turbulent transport is either calculated by trapped-gyro-Landau-fluid (TGLF) [24, 25], a gyrofluid and electromagnetic QL model with shaped flux surfaces, or by QuaLiKiz (QLK)[26, 27], a gyrokinetic and electrostatic QL transport model with circular flux surfaces. Specifically, we employed the most recent versions of the models: TGLF SAT2, characterised by a fit of the geometrical coefficients to 3D CGYRO spectra and by an agreement with CGYRO non-linear simulations described in [25], and the last release of QLK, featuring enhancements in the trapped electron mode (TEM) treatment described in [27].

The JINTRAC suite with the JETTO transport solver was used for full physics DTT simulations using the QLK model, while the TGLF runs were performed adopting the ASTRA–JINTRAC scheme described in [7]. The stable numeric scheme used for the QL transport models is described in [28]. In addition to the main turbulent transport, a small contribution (3%) of Bohm transport is used to ensure the numerical stability to the computation even when all other transport terms become too small. Furthermore, since the neoclassical electron heat transport results rather insignificant close to the plasma centre, an additional electron diffusivity of $\chi = 0.5\,\mathrm{m^2\,s^{-1}}$ is added within $\rho_{tor} = 0.2$.

In the pedestal region, the kinetic profiles of the two main species are kept fixed, using the pedestal top values of temperatures and densities as boundary conditions of our core simulations, and $T_e = T_i$ is assumed. The pedestal profiles

were previously determined by specific runs of Europed code [29] using the EPED1 model [30], for each scenario. In the Europed runs, pedestal height and width are determined by identifying the intersection between the peeling-ballooning constraint and the kinetic ballooning mode constraint. More details are described in [7, 30].

A good agreement among SOL, pedestal, and core steady-state simulations ensures a high confidence level in the modelling results. Hence, properly defining all simulation settings and all parameters to use for the pedestal characterisation in order to be compatible with detachment conditions imposed by the SOL calculations [8, 12] has been crucial. For every Europed simulation, we prescribed a certain seeding impurity and we set input values in agreement with the SOL modelling requirements for the effective charge $Z_{\rm eff} = \sum_i Z_i^2 n_i/n_e$ in the pedestal, the temperature at the separatrix $T_e^{\rm sep}$, and the relative shift defined as the distance between the positions of the pedestal temperature and density $(T_e^{\rm pos} - n_e^{\rm pos})$. Setting a value to the relative shift implies setting the density at the separatrix $n_e^{\rm sep}$. Moreover, in the pedestal modelling, the magnetic equilibrium is specified, the electron density at the pedestal top $n_e^{\rm ped}$ is set to obtain a Greenwald fraction of $\bar{n}_e/n_{\rm Gr} \approx (0.45 - 0.55)$ in the core runs, and a tuned $\beta_{\rm pol}$ value is used to match with the JINTRAC predictions. Europed does not consider directly the effect of neutrals. However, this effect is considered indirectly by using $n_e^{\rm sep}/n_e^{\rm ped}$ as an input parameter. In fact, as shown in [31–34], $n_e^{\rm sep}$ is a parameter that in first approximation can describe well the effect of the neutrals in the pedestal.

We underline that, even if the pedestal region is included both in the core and SOL modelling, only the Europed simulations properly model the pedestal pressure profile. Thanks to the overlapping of the core and SOL modelling regions, the key parameters in the pedestal region and at the separatrix can be compared.

In the core modelling, two impurities are always included: a seeding impurity (argon, neon, or nitrogen), used to increase the radiative dissipation reducing the divertor power load, and tungsten ($A \approx 184$, $Z = 74$) coming from the FW and the divertor. In the JINTRAC runs, the SANCO code [35] calculates impurity densities and radiation up to the separatrix, treating all ionisation states separately. To conserve the particle number during the simulation, we set the recycling factor, the escape velocity, and the neutral influx as null; the decay lengths are set equal to $\lambda_n = \lambda_T = 1.0$ cm, in agreement with the SOL simulations. Setting a radially constant effective charge $Z_{\rm eff}$ and an impurity density ratio $n_{\rm W}/n_{\rm seed.imp.}$ as SANCO initial conditions entails certain concentrations of the seeding impurity and tungsten during the run, tuned to be compatible with typical values in tokamaks operating in full detachment [36] and with SOL modelling predictions.

During the JINTRAC simulations, the fixed boundary equilibrium solver ESCO updates the MHD equilibrium three times per second, keeping fixed the plasma boundary to the reference shape described in [37] and provided by the free boundary solver CREATE-NL [38]. The magnetic-separatrix shape of the SN DTT scenario at the full current and full field operational point is shown in figure 1.

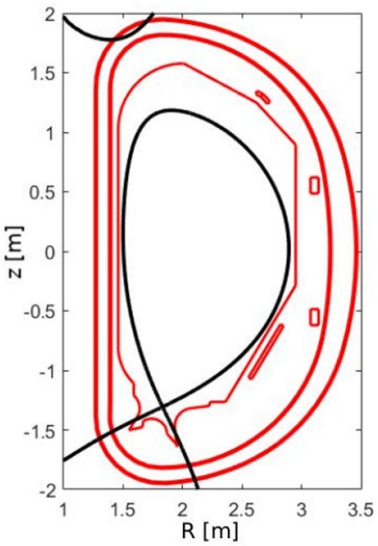

Figure 1. Sketch of the DTT poloidal section (in red) with the SN scenario magnetic-separatrix shape (in black).

A theory-driven empirical model [39, 40] has been employed to predict the toroidal rotation. Based on the pinch number dependence on some plasma parameters discussed in [40], we built a pinch number RV_ϕ/χ_ϕ null at the plasma centre, equals to $\sim$2.5 at $\rho_{\rm tor} = 0.4$, and with the trend $RV_\phi/\chi_i \propto -\sqrt{r/R}$ to include the inward momentum pinch. The momentum transport coefficient χ_ϕ is substituted by the product between the ion thermal transport coefficient χ_i and a Prandtl number value $\chi_\phi/\chi_i = 0.7$ lower than the unit to consider the residual stress due to $E \times B$ shearing. Observing DTT from above, the plasma rotation is counter-clockwise, i.e. co-current (according the sign convention used here, $\omega_{\rm tor}$ has negative values). In the pedestal region, the rotation has been arbitrarily supposed to move from zero up to $|\omega_{\rm tor}| = 10\,{\rm krad\,s^{-1}}$, that is a reasonable assessment based on measurements in present tokamaks. Anyway, the simulation is not significantly affected by this assumption, but rather by the rotation gradient.

The implementations in JINTRAC of the ECRH, ICRH, and NBI systems have been updated to their new set-up designed for the present DTT configuration, so that the heating and current drive systems as well as the NBI particle source could be simulated self-consistently during the JINTRAC runs, accounting also for the synergy effects.

The ECRH system includes up to 32 gyrotrons at 170 GHz, split in 4 clusters, with an installed power of 1 MW from each gyrotron. Every cluster is composed by two upper (UP) gyrotrons, three equatorial top (EQT) gyrotrons, and three equatorial bottom (EQB) gyrotrons, depending on the access port. The ECRH power deposition is calculated four times per second by the GRAY code [41], considering at the most 20 different beams and modelling each beam as sum of one central ray and 160 rays arranged on 10 concentric rings evenly distributed between the beam axis and the beam radius, at which the wave electric field amplitude is $1/e$ times the on-axis value.

DTT will also be equipped with a negative ion based NBI system with a single injector able to inject up to 10 MW of power into the plasma. The deuterium beam is designed to reach an energy $\leqslant$510 keV, to operate effectively at high densities [42]. The injector installation is planned for the 2032. The NBI system is modelled by the PENCIL code [43], setting all beam particles injected at the nominal energy due to the negative ion source. As described in detail in [44], the sum of prompt and ripple NBI fast particle losses is $\sim$4% only and we could neglect them in our modelling work.

Every modular unit of the ICRH system is composed by a pair of three-strap RF antennas located in an equatorial port and operating in the frequency range 60–90 MHz, with an installed power of 2 MW from each antenna. Up to 2 ICRH modules, i.e. up to 4 RF antennas, will be installed on DTT. The ICRH power deposition and the synergy effects with NBI are computed by the PION code [45] in the performed runs. In the simulations with ICRH of this paper, a RF frequency of 90 MHz and a concentration of 5% hydrogen as minority species are always set, so that the cyclotron resonance is placed where the magnetic field is $B_{\rm tor} \approx 5.9$ T.

The total neutron rate, which is due to the sum of neutron production from fusion reactions between two thermal nuclei, between a thermal nucleus and a fast nucleus of the NBI beam, and between a thermal nucleus and a fast nucleus of the ICRH minority species, is also computed during the JINTRAC runs. This assessment is useful to guarantee that the designed neutron shields will be able to cope with DTT neutron loads.

For the first time, an investigation of the sawteeth in DTT has been carried out using the Porcelli model [13]. These simulations are described in section 2.2.2. In the other sections, the simulations do not include sawteeth and hence their profiles have to be interpreted as related to the saturated recovery after a sawtooth crash.

ELMs are not included in the modelling yet, but first estimations of their impact on the full power scenario predictions through suitable scalings [14–17] are discussed in 2.2.3.

2.2. The E1 scenario

The E1 scenario works at the full current and full field operational point, i.e. with plasma current of $|I_{\rm pl}| = 5.5$ MA and vacuum toroidal magnetic field of $B_{\rm tor} = 5.85$ T.

The reference heating option selected in [7] for the DTT E1 scenario, corresponding to the full power scenario, foresees:

- 32 gyrotrons to provide a total ECRH power to the plasma of about 28.8 MW (as a result of 32 MW of installed power and an estimated loss factor before launchers of 0.1), injecting beams in O-mode;
- 4 RF antennas split in 2 modules to provide a total ICRH power to the plasma of about 6.0 MW (as a result of 9 MW of installed power and an efficiency of 0.75 due to transmission lines and antenna coupling);
- 1 NBI with 510 keV to provide a total NBI power to the plasma of about 10.0 MW.

Being too numerous to be modelled separately, the 32 gyrotrons have been assembled into subsets: 12 different ECRH beams are simulated by GRAY.

In relation to the EC launcher positioning of [46], the toroidal angles have been set in the following ranges: $(-5.0^\circ) - (-4.5^\circ)$ for UP beams, $(-4.0^\circ) - (+0.5^\circ)$ for EQT beams, and $(+1.0^\circ) - (+2.5^\circ)$ for EQB beams. The poloidal angles have been set in the following ranges: $(+42.5^\circ) - (+44.5^\circ)$ for UP beams, $(-5.5^\circ) - (-1.0^\circ)$ for EQT beams, and $(-2.5^\circ) - (+2.5^\circ)$ for EQB beams. With these angle settings, a high ECRH power density is deposited in the central region $0.1 \leqslant \rho_{\rm tor} \leqslant 0.35$ of the plasma.

For the E1 scenario, a comparative analysis between two possible seeding impurities (argon or neon) has been done with both core and SOL [8] modelling.

In JINTRAC simulations with argon (Ar, $A \approx 40$, $Z = 18$), we set $Z_{\rm eff} = 1.8$ and $n_{\rm W}/n_{\rm Ar} = 0.01$ as SANCO initial conditions, while in runs with neon (Ne, $A \approx 20$, $Z = 10$) we set $Z_{\rm eff} = 2.2$ and $n_{\rm W}/n_{\rm Ne} = 0.04$.

Obviously, the Europed modelling has been also repeated to obtain the pedestal pressures with argon and with neon, setting the same values of effective charge used in SANCO as initial conditions. Temperatures at the separatrix of $T_e^{\rm sep} = T_i^{\rm sep} =$ 130 eV, a pedestal top density of $n_e^{\rm ped} = 1.4 \times 10^{20}$ m^{-3}, a value of $\beta_{\rm pol} = 0.55$, and a relative shift of $(T_e^{\rm pos} - n_e^{\rm pos}) = 0.0125\psi_N$ in order to have $n_e^{\rm sep} \approx 0.8 \times 10^{20}$ m^{-3} have been set as inputs of these E1 Europed runs, predicting pedestal top temperatures of about 1.6 keV and 1.7 keV in the cases with argon and with neon respectively. The $\langle n_e \rangle_{\rm sep} \approx 0.8 \times 10^{20}$ m^{-3} is the minimum density that allows sustainable steady-state divertor conditions in the E1 scenario with reasonable values of the effective charge at the separatrix $\langle Z_{\rm eff} \rangle_{\rm sep}$.

Thus, the core integrated modelling of the E1 scenario has been performed with both argon and neon as seeding impurity and using both TGLF and QLK as turbulent transport model. For the E1 runs, the transport equations have been always solved within $\rho_{\rm tor} = 0.94$.

Table 2 shows the main modelling settings and results of SOL and core modelling of the E1 scenario: the effective charge at the pedestal top $Z_{\rm eff}^{\rm ped}$, the effective charge at the separatrix $Z_{\rm eff}^{\rm sep}$, the electron density at the pedestal top $n_e^{\rm ped}$, the seeding impurity concentration at the pedestal top $C_{\rm seed.imp.}^{\rm ped} = n_{\rm seed.imp.}^{\rm ped}/n_{\rm D}^{\rm ped}$, the tungsten concentration at the pedestal top $C_{\rm W}^{\rm ped} = n_{\rm W}^{\rm ped}/n_{\rm D}^{\rm ped}$, and the amount of power radiated in the region $0.85 < \rho_{\rm tor} < 1.0$.

Some discrepancies between core and SOL simulations are due to the different modelling approaches and to the numerous input parameters. However, a good compatibility is obtained between SOL and core simulations of the E1 scenario, taking into account that the core simulations include two impurities whilst the SOL simulations include only the seeded impurity. The uncertainty on tungsten concentration leads to uncertainty on the power crossing the separatrix with a given main impurity concentration; this could lead to different divertor plasma states. Other differences may be given by the transport model used, the tuning of transport parameters, the inclusion of pinches, and the treatment of impurity transport.

Table 2. Comparison between SOL and core modelling main results for the E1 scenario.

	SOL modelling	Core modelling TGLF	Core modelling QLK	SOL modelling	Core modelling TGLF	Core modelling QLK
Seeding impurity	Ne	Ne	Ne	Ar	Ar	Ar
$Z_{\rm eff}^{\rm ped}$	2.6–3.2	1.7	2.4	2.2–3.0	1.4	2.0
$Z_{\rm eff}^{\rm sep}$	3.0–4.2	2.3	3.9	2.0–3.6	2.0	3.5
$n_e^{\rm ped}$ $(10^{20}/{\rm m}^3)$	1.5–1.7	1.4	1.4	1.5–2.1	1.4	1.4
$C_{\rm seed.imp.}^{\rm ped}$ (10^{-2})	4.0–15.6	1.6	3.9	0.5–2.9	0.4	1.2
$C_{\rm W}^{\rm ped}$ (10^{-5})	—	5.0	1.0	—	2.4	6.0
$P_{\rm rad}$ (MW) $[0.85 < \rho_{\rm tor} < 1.0]$	6.5–8.8	4.5	8.8	5.3–10.0	3.0	6.4

We also notice from table 2 that argon requires slightly lower effective charge and lower power radiated within the separatrix than neon to obtain detached divertor plasma. Nevertheless, with both seeded impurities it is possible to obtain detached condition with more than 20 MW crossing the separatrix which is a condition for H-mode operations. A work on core-pedestal-SOL-integrated modelling, totally self-consistent in terms of temperature and density profiles, fluxes, and transport coefficients, can be envisaged as future development.

In table 2 we reported a range of argon or neon content predicted by SOL modelling. The motivation of this range is the difference of final results than can be obtained from edge modelling depending on initial detached or attached conditions. In high seeded, high density, high radiation simulations we observed a hysteretical behaviour which was described in [8].

The radial profiles of electron temperature T_e, ion temperature T_i, electron density n_e, toroidal rotation $\omega_{\rm tor}$, safety factor absolute value $|q|$, seeding impurity density $n_{\rm seed.imp.}$, tungsten density $n_{\rm W}$, effective charge $Z_{\rm eff}$, radiative power density $Q_{\rm rad}$, and radiative power $P_{\rm rad}$ obtained by the four core runs are shown in figure 2. In figures 3(a) and (b), there are respectively the radial profiles of all power densities and of the total electron and ion powers, only for the TGLF case with argon since the power density and total power profiles related to the other three simulations are similar in shape and size.

We note from figure 2(b) that impurities do not accumulate in the centre significantly. Nonetheless, the effect of differences in electron and deuterium profiles according to the used transport model reflects on the impurity densities considerably. As discussed before, the effective charge values listed in table 2 ($Z_{\rm eff}^{\rm ped} = 1.4 - 2.4$ and $Z_{\rm eff}^{\rm sep} = 2.0 - 3.9$) cover a broad range and are quite compatible with the SOL modelling values.

From figure 2(a), we notice that the temperature profiles are quite in good agreement, with the exception of the QLK run with neon. Some discrepancies arise in the density profiles, due to both the differences in the impurity profiles and the change of turbulent transport model. The different predictions in electron density profiles by QLK and by TGLF are a known question, already dealt with for the old DTT configuration, as extensively discussed in [7]. Especially the excessive n_e flatness in the inner region of the plasma, such as in the present QLK run with neon, is not validated, as found by a comparison of QLK stand-alone runs with gyrokinetic results obtained by the GENE code [47, 48] reported in [7]. Although the TGLF results should be more reliable, both QL models should be approached with care inside $\rho_{\rm tor} = 0.4$, where the power density is very high and the $|q|$ profile is quite lower than 1 in these simulations without sawteeth. Excluding the unlikely case with QLK and neon, $T_{e_0} \approx 15.5$–19.0 keV, $T_{i_0} \approx 8.9$–11.7 keV, and $n_{e_0} \approx (2.05 - 2.35) \times 10^{20}\,{\rm m}^{-3}$ values are reached at the plasma centre.

In any case, the electron temperature results much larger than the ion temperature over almost all plasma radius. Notwithstanding the high thermal exchange power due to the collisional coupling P_{ei} flowing from electrons to ions, the ion temperature profile is unable to grow, because the ion temperature gradient mode (ITG) threshold is low for $T_e/T_i > 1$ and a strong ion stiffness is predicted by the turbulent transport model. We highlight that the E1 scenario has been found to be dominated by the ITG modes over all the radial profile. Raising the electron density in order to strengthen the collisional coupling could be an attempt to balance more T_e and T_i, although limited by the ECRH cut-off at $n_e = 3.58 \times 10^{20}\,{\rm m}^{-3}$. Nevertheless, since the ITG threshold is weakly dependent on the temperature ratio when $T_e/T_i > 1$, this would lead to a decrease of T_e rather than a T_i gain.

As shown in figure 3, we notice that the ohmic power $P_{\rm Ohm} \approx 0.8 - 1.1$ MW is quite negligible, the core radiated power $P_{\rm rad} \approx 12.8 - 16.1$ MW is around the 29%–36% of the total power, and a huge amount of collisional power $P_{ei} \approx 18.6 - 21.9$ MW flows from electrons to ions.

In figure 4, the radial profiles of the neutron density rate and of its three contributions as well as of the integrated neutron rate are displayed for the QLK case with argon. Similar trends of neutron contributions can be observed in all E1 simulations: in any case, the thermal–thermal and the thermal-beam components are dominant. The total neutron rate results in the range $(0.9$–$1.3) \times 10^{17}$ neutrons s^{-1}. This order of neutron loads can be easily withstood by the neutron shields currently planned for DTT.

In figure 5, radial profiles of the particle and energy densities of the energetic ions are displayed for the run with TGLF and argon. Similar profile shapes has been found for the other E1 cases. The energetic particles, which are due to the NBI and

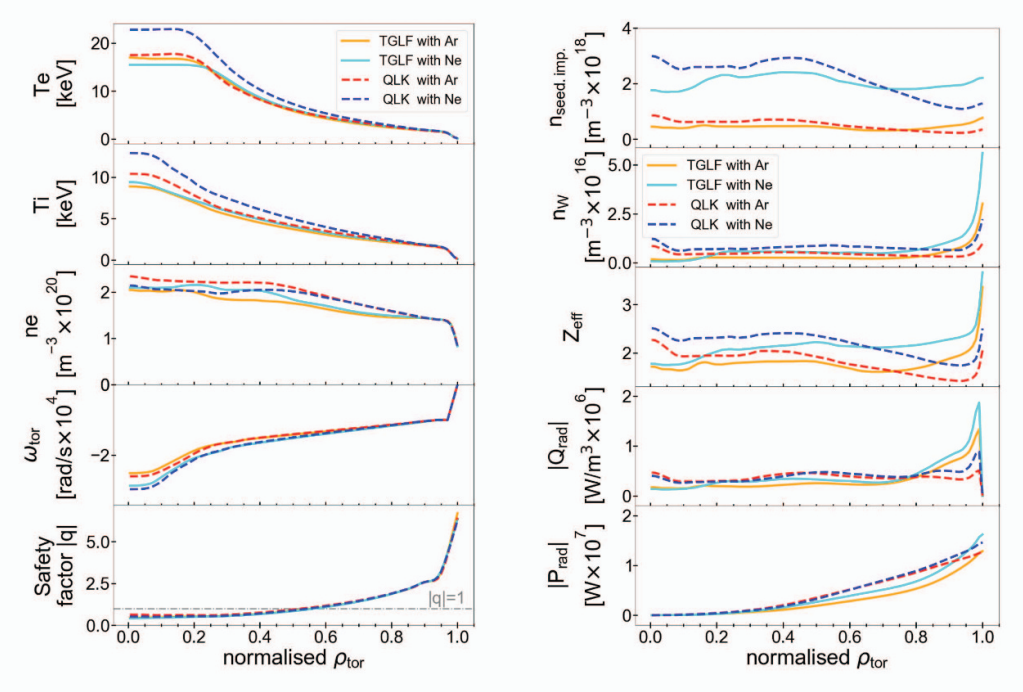

(a) (b)

Figure 2. Radial profiles for the E1 scenario flat-top phase (a) of the electron and ion temperatures, electron density, toroidal rotation, and safety factor absolute value and (b) of the seeding impurity and tungsten densities, effective charge, radiative power density, and radiative power, with turbulent transport calculated by TGLF SAT2 (solid lines) or by QLK (dashed lines) with argon (reddish lines) or with neon (blueish lines).

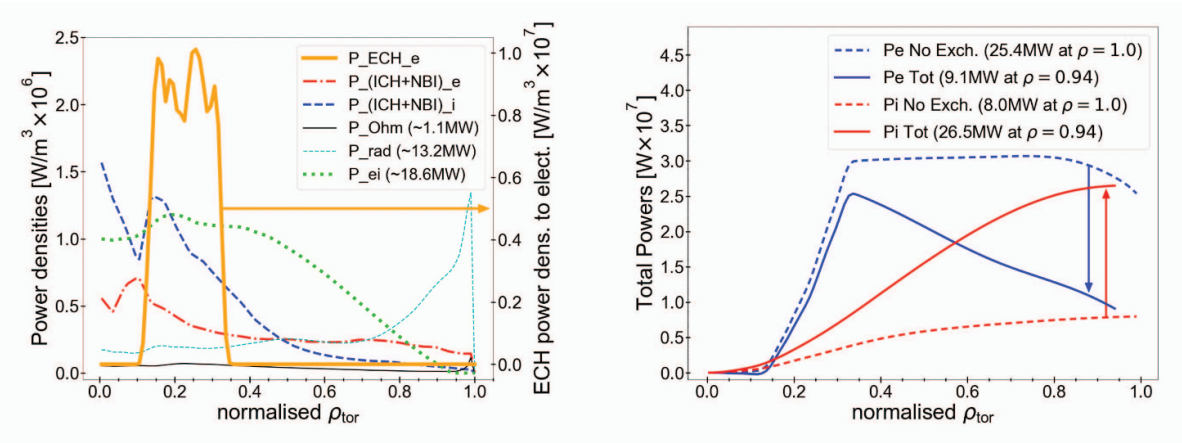

(a) Power densities. (b) Volume integrated powers.

Figure 3. (a) Radial profiles for the E1 scenario of power densities: ECRH power deposited to electrons $P_{\mathrm{ECRH}e}$, NBI and ICRH power deposited to electrons $P_{(\mathrm{ICRH+NBI})e}$, NBI and ICRH power deposited to ions $P_{(\mathrm{ICRH+NBI})i}$, Ohmic power P_{Ohm}, radiative power P_{rad}, and thermal exchange power between electrons and ions P_{ei}. (b) Radial profiles for the E1 scenario of electron and ion total powers including or not including the thermal exchange power between species. All these profiles of E1 scenario refer to the TGLF case with argon.

ICRH systems, own an energy amount in the range of 5%–7% of the total plasma energy.

The radial profiles of current densities are shown in figure 6 (negative values indicate a current density flowing in the opposite direction of the toroidal magnetic field). They refer to the run with TGLF and argon, but all other cases exhibit alike profiles. The total current density J is mainly due to the inductive contribution.

In the examined core simulations of the E1 scenario, triangularity values in the range $\delta_{95} = 0.31 - 0.33$, elongation values in the range $\kappa_{95} = 1.62 - 1.64$, and safety factor values in the range $|q_{95}| = 2.7 - 2.9$ have been calculated at the flux surface which contains the 95% of the poloidal flux. In the present DTT configuration the $|q_{95}|$ value is close to 3, larger than in the previous machine design [7], reducing therefore the disruption risk [49].

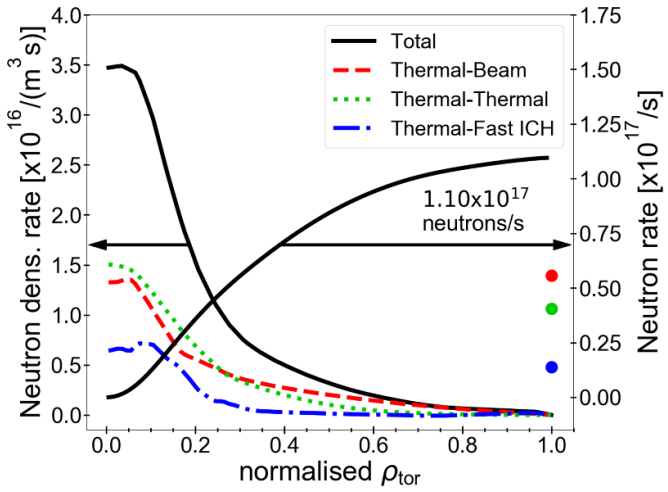

Figure 4. Radial profiles for the E1 scenario of neutron density rates, where neutrons are produced by fusion reactions between: two thermal nuclei (green), between a thermal nucleus and a fast nucleus of the NBI beam (red), and between a thermal nucleus and a fast nucleus of the ICRH minority species (blue), any pair of nuclei (black). The radial profile of the total neutron rate is also displayed (black), with points indicating the three contributions to it. These profiles of the E1 scenario refer to the QLK case with argon.

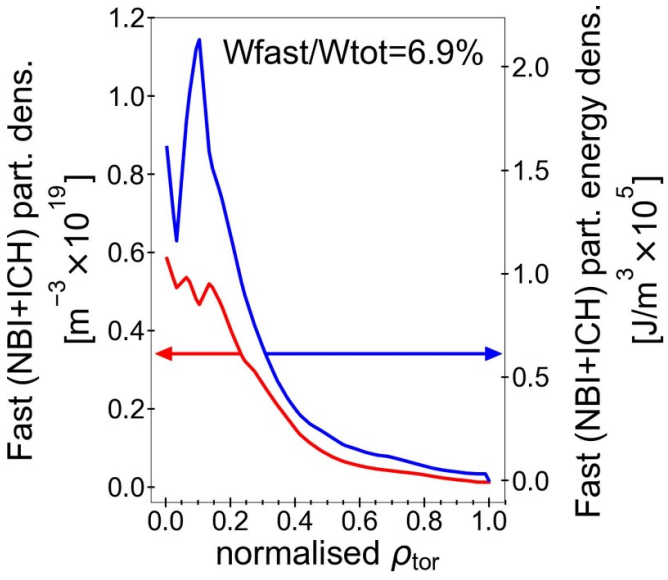

Figure 5. Radial profiles for the E1 scenario of density and energy density of energetic particles due to the NBI and ICRH systems. These profiles of the E1 scenario refer to the TGLF case with argon.

Furthermore, for these E1 simulations, an energy confinement time and an H-factor (with $P = P_{sep}$) respectively equal to $\tau_E = (0.3 - 0.5)$ s and $H_{98} = 0.8 - 1.1$ have been calculated.

2.2.1. EC current drive and power deposition. The safety factor radial profiles of the E1 scenario flat top phase are characterised by $|q| = 1$ located in the outer half of the plasma ($\rho_{tor} \approx 0.53 - 0.58$) and by inner values of $|q|$ significantly lower than 1 (with $|q_0| \approx 0.5$), as observed in figure 2(a). Such profiles indicate strong $n = 1$ $m = 1$ ideal MHD activity and

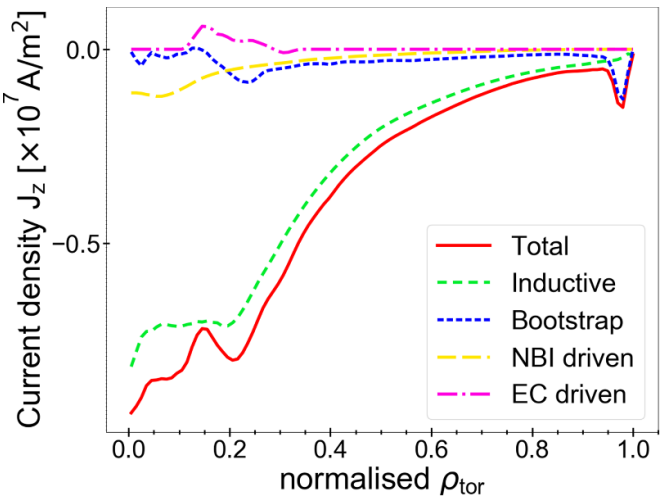

Figure 6. Radial profiles of current densities in the SN E1 scenario: total current J, inductive current J_{ind}, bootstrap current J_{BS}, NBI drive current J_{NB}, and EC drive current J_{EC}.

as such sawtooth crashes would likely take place before these conditions are reached. It would affect a wide plasma region, and then the whole plasma evolution. Therefore, from one side we started to integrate the sawteeth evolution in the DTT E1 scenario simulations, as described in section 2.2.2, and, on the other side, we performed an initial study regarding the tailoring of the q profile by varying the EC current drive (ECCD) and the EC power deposition localisation, as discussed in this section. The aim of the analysis here reported is to investigate the possibility of lowering the $|q| = 1$ radial location ρ_1 and guarantee that it does not exceed $\rho_{tor} = 0.5$, thus reducing the crash extension and improving the scenario against the effect of the sawtooth oscillations. In order to achieve such purpose, the EC current can be driven to increase the q values in the plasma region characterised by $|q| < 1$, or to decrease the q values outside ρ_1, lowering then the slope of the q profile in the inner region.

Exploiting the wide flexibility of the EC system, we tested different angle sets for DTT gyrotrons, included some drastic cases (e.g. with depositing the whole power extremely outside), in order to investigate how much ECRH&ECCD could affect the safety factor in this scenario. Thus, simulations have been carried out setting the EC launching angles in order to test both inner EC localisation ($\rho_{tor} < 0.5$) with counter-ECCD, with the aim of increasing the q values in the inner half of the plasma, and outer EC deposition with co-ECCD, in order to lower the q gradient in the region outside the $|q| = 1$ location.

The ECCD effects on q profile resulted negligible with a counter-current inside $\rho_{tor} = 0.5$ and quite small with a co-current outside $\rho_{tor} = 0.5$. It is not surprising, since the EC current and the other non-inductive currents are significantly lower than total current, as displayed in figure 6. The major impact is actually due to the power deposition location, which deeply modifies the electron temperature gradient and the conductivity. However, a co-ECCD with EC localisation outside $\rho_{tor} = 0.5$ has been found to be only slightly beneficial on $|q| = 1$ placement.

After a trade-off work, we selected a feasible and reasonable set of EC launching angles which guarantees higher performance with a better q profile.

In relation to the EC launcher positioning of [46], the toroidal angles have been set in the following ranges: -25.0° for UP beams, $(+17.0^\circ)-(+25^\circ)$ for EQT beams, and $(+14.5^\circ)-(+24.5^\circ)$ for EQB beams. The poloidal angles have been set in the following ranges: $(+40.0^\circ)-(+42.0^\circ)$ for UP beams, $(-15.0^\circ)-(-8.0^\circ)$ for EQT beams, and $(-10.0^\circ)-(-6.0^\circ)$ for EQB beams. With these settings, the ECRH power density is spread between $0.05 \leqslant \rho_{\rm tor} \leqslant 0.7$, as shown in figure 7.

The electron density and the ion temperature profiles are barely affected in a small region close to the plasma centre by this EC deposition displacement.

The electron temperature instead is considerably reduced within $\rho_{\rm tor} \approx 0.3$, although the central value $T_{e0} \sim 10\,$keV is still high. Thanks to this new ECRH distribution, the $|q| = 1$ location moves inward of about $\Delta\rho_{\rm tor} \approx 0.05$ (from $\rho_{\rm tor} \approx 0.53$ to $\rho_{\rm tor} \approx 0.48$). Although it is a small improvement, actually it impacts significantly and positively on the sawteeth and, hence, on the plasma stability.

In addition, such spread EC power deposition implies relevant advantages for the fuelling efficiency of the DTT pellets, as examined in [50].

On the other hand, an outer ECRH power deposition could lead to a risky tungsten accumulation in the plasma centre and hence should be handled carefully. As shown in figure 8, we verified that for the new gyrotron settings the central W density does not grow too much.

2.2.2. Sawteeth. An analysis of the sawtooth impact on the E1 scenario kinetic profiles and on the safety factor has been carried out for the first time in DTT. Specifically, sawteeth have been included into the JINTRAC simulation with QLK as turbulent transport model, with argon as seeding impurity and with a spread ECRH power deposition, described in the previous section 2.2.1.

In spite of the safety factor enhancement due to the new set of gyrotron angles described in section 2.2.1, the low value of $|q_{95}|$ and the $|q|$ profiles shown in figure 7 suggest an important sawtooth activity.

The Porcelli sawtooth crash trigger model discussed in [13], and integrated in the code suite, has been used for the identification of the instability onset. The coefficients related to the four implemented stability criteria have been set to the default values $C_f = C^* = C_\rho = 1$ and $C_h = 0.4$. Particularly, C_f multiplies the contribution of fast ion energy, C_ρ is a numerical factor multiplying the thermal Larmor radius in the ion-kinetic regime, C^* quantifies the role of the ion and electron diamagnetic frequency in the ST stabilisation associated to the kink growth rate, and finally C_h quantifies the role of the fast ion energy on the ST stabilisation with respect to the core plasma potential energy. When the instability onset condition of the trigger model is met during the evolution of the profiles, a reconnection model is used to predict the relaxed temperature, density, and $|q|$ profiles after a sawtooth crash.

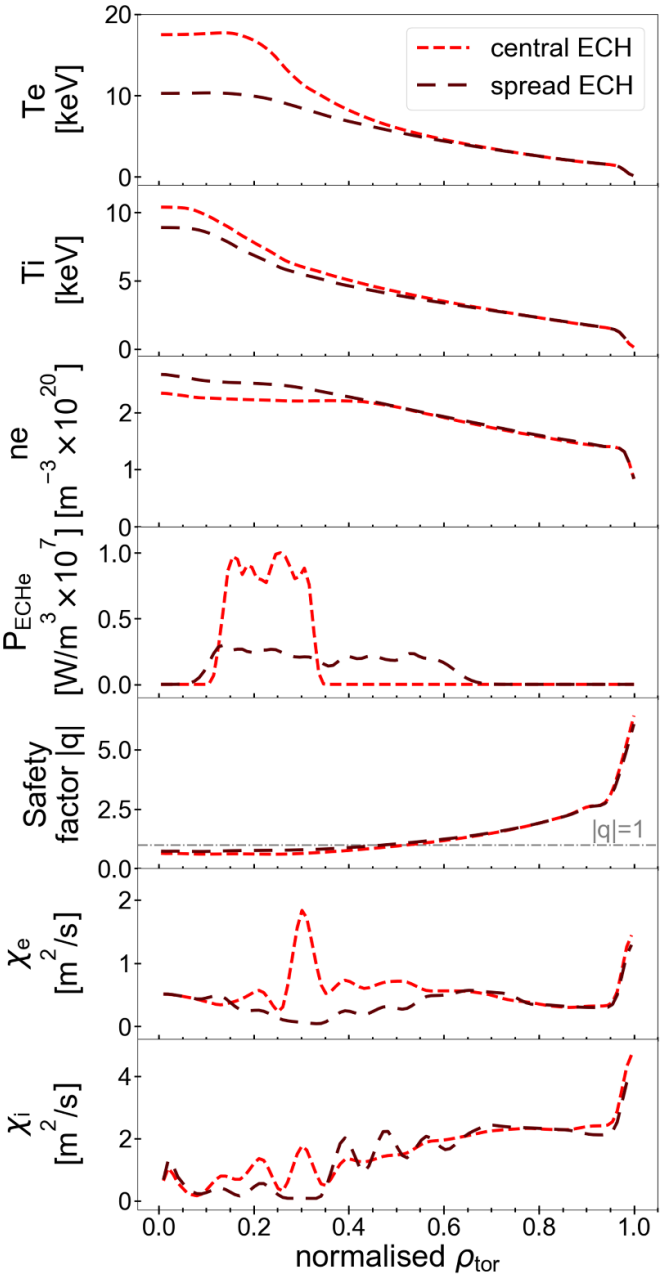

Figure 7. Comparison of electron temperature, ion temperature, electron density, ECRH power density, safety factor, electron heat diffusivity χ_e, and ion heat diffusivity χ_i radial profiles using different gyrotron angles. These profiles refer to the QLK cases with argon.

Initially, the Kadomtsev complete reconnection model [51, 52] has been employed. Therefore, the relaxed $|q|$ profile flattens to unity up to the mixing radius $\rho_{\rm mix} \approx 0.55$, which describes the portion of plasma involved in the reconnection process and which is somewhat larger than $\rho_1 \approx 0.45$, as shown in figure 9(a). The electron temperature evolution, displayed in figure 9(b), shows clearly sawtooth oscillations.

This simulation with a complete reconnection foresees a long sawtooth period of about 0.72 s (i.e. $f_{\rm ST} \approx 1.4\,$Hz) because of the stabilising effect of the fast particles coming from the ICRH and NBI heating systems. With a complete

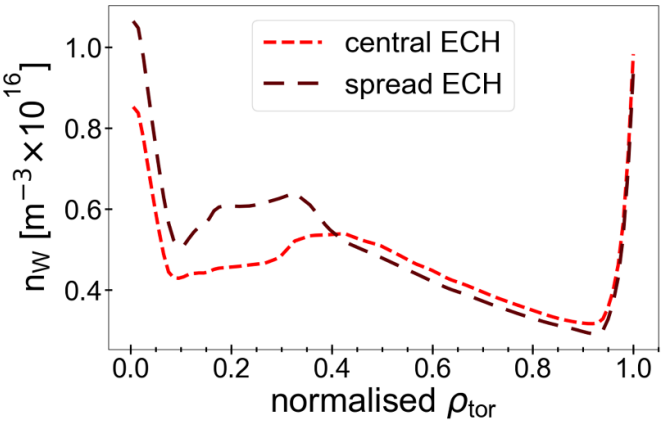

Figure 8. Comparison of tungsten density radial profile using different gyrotron angles. These profiles refer to the QLK cases with argon.

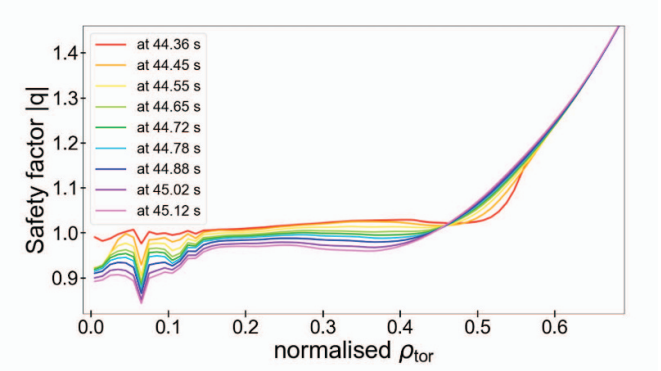

(a) Relaxation of the $|q|$ profile.

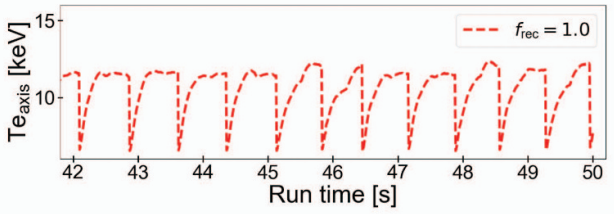

(b) Time evolution of T_{e_0}.

Figure 9. Time evolution (a) of the $|q|$ profile after a sawtooth crash and (b) of the electron temperature at the plasma centre T_{e_0}, using a complete reconnection model (i.e. with $f_{rec} = 1.0$).

reconnection, the predicted crash amplitude of ~ 5.1 keV is also quite large, with a drop of the central temperature of 44%. This result was expected since a ρ_1 close to $\rho_{tor} = 0.5$ entails a mixing radius ρ_{mix} in the outer half of the plasma, which means a very large portion of the plasma involved in the reconnection process.

On the other hand, it is well known that the complete flattening of the $|q|$ profiles described by the basic Kadomtsev reconnection model does not always occur experimentally, and $|q_0|$ can stay below 1 after the crash. The large $|q| = 1$ radius predicted for the E1 scenario in the previous section is an indication that the same could happen for DTT [53, 54].

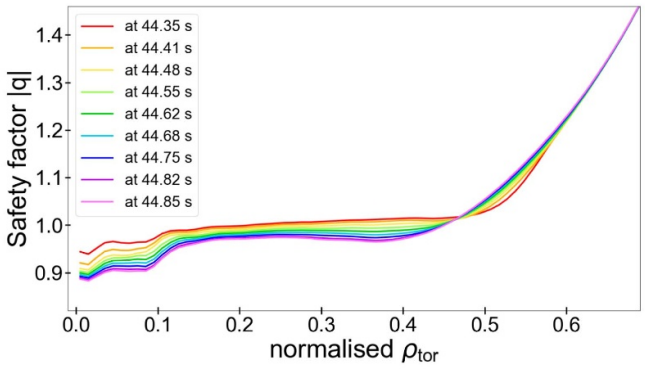

(a) Relaxation of the $|q|$ profile.

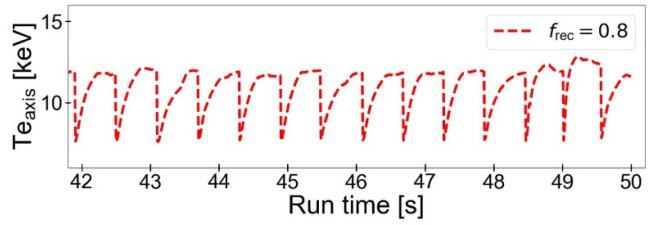

(b) Time evolution of T_{e_0}.

Figure 10. Time evolution (a) of the $|q|$ profile after a sawtooth crash and (b) of the electron temperature at the plasma centre T_{e_0}, using an incomplete reconnection model with $f_{rec} = 0.8$.

Such situation can be modelled considering a very simple 'incomplete' Kadomtsev reconnection, where the relaxed profile is a weighted average between the pre-crash and the completely reconnected post-crash profiles. The weight is the reconnection fraction parameter f_{rec}, where a complete reconnection corresponds to $f_{rec} = 1$.

Therefore, we repeated the simulation described so far, but employing an incomplete reconnection with a value of $f_{rec} = 0.8$.

From figure 10(a), where the $|q|$ profile relaxation after a sawtooth crash predicted is shown, we notice that the q_0 value remains always below 1 in this new run, as expected. Figure 10(b) displays the electron temperature evolution for this case with $f_{rec} = 0.8$, resulting in a sawtooth period of 0.59 s (i.e. $f_{ST} \approx 1.7$ Hz) and a crash amplitude of 4.2 keV. The effect of the incomplete reconnection relaxation on the sawtooth activity predictions is a shortening of the sawtooth period and a reduction of the crash amplitude, however, the central temperature drop is still about 35%.

In summary, this first analysis predicts an important sawtooth activity for the described E1 scenario flat-top phase, mainly due to the large ρ_1. The mixing radius larger than half radius also suggests that an incomplete reconnection is likely to take place as relaxation process. The incomplete reconnection changes the sawtooth impact increasing its frequency, so predicting plasma scenario less prone to the onset of MHD instability as the neoclassical tearing modes which can lead to loss of confinement [55]. Describing the

incomplete reconnection relaxation by a more accurate reconnection model could also obtain a beneficial reduction of the ρ_1 during sawtooth oscillations.

Therefore, simulations considering a more accurate incomplete reconnection model, like the one discussed in [13], are planned for the future.

2.2.3. ELMs. In this section, the main features of type-I ELMs are derived for the reference DTT E1 scenario using existing scalings. This will serve as guideline for future edge and plasma wall-interaction studies which are strongly impacted by type-I ELMs in H-mode.

Plasma profiles and values of the TGLF simulation with argon and central ECRH reported in section 2.2 were used here as reference case. Since the employed scalings only depend on pedestal parameters, the choice of a specific run actually does not affect the results.

To evaluate the impact of type-I ELMs on DTT, the approach in [56] is followed. Type-I ELMs decrease the plasma energy by typically $\Delta W_{\rm ELM}/W_{\rm ped} = 3\%$–$20\%$, where $W_{\rm ped}$ is the pedestal energy, in timescales of few hundred μs in present divertor tokamaks. $\Delta W_{\rm ELM}$ and $W_{\rm ped}$ are defined as follows:

$$\Delta W_{\rm ELM} = (3\langle n_{\rm ped}\rangle \Delta T_{\rm ped,ELM} + 3\langle T_{\rm ped}\rangle \Delta n_{\rm ped,ELM}) V_{\rm ELM} \quad (1)$$

$$W_{\rm ped} = 3 n_{\rm ped} T_{\rm ped} V_{\rm plasma} \quad (2)$$

where $V_{\rm ELM}$ is the volume of plasma affected by the ELM, $\Delta n_{\rm ped,ELM}$ and $\Delta T_{\rm ped,ELM}$ are the density and temperature drops at the pedestal top caused by the ELMs, and $V_{\rm plasma}$ the total plasma volume. A multi-machine scaling shows that $\Delta W_{\rm ELM}/W_{\rm ped}$ is a function of the normalised pedestal collisionality $\nu^* \approx 0.46\, q_{95} R(\mathrm{m})/\ \mathrm{T(keV)}$ (see figure 11) [14]. The reference E1 scenario of DTT has a normalised pedestal collisionality (at $\rho_{\rm tor} = 0.94$) of about $\nu^*_{\rm DTT} = 0.23$ and hence $\Delta W_{\rm ELM}/W_{\rm ped} \approx 9.6\%$. Given $W_{\rm ped} = 3.56\,$MJ, $\Delta W_{\rm ELM} = 0.34\,$MJ.

The relative energy loss during type-I ELMs is then used to determine the maximum energy fluence to the outer divertor $\epsilon_{\parallel}^{\rm peak}$ in MJ m^{-2} using the scaling proposed in [15], expressing $n_{e,\rm ped}$ in [10^{20} m^{-3}], $T_{e,\rm ped}$ in [keV], $\Delta W_{\rm ELM}$ in [%], and $R_{\rm geo}$ in [m]:

$$\epsilon_{\parallel}^{\rm peak} = 0.28 \pm 0.14 \cdot n_{e,\rm ped}^{0.75\pm0.15} T_{e,\rm ped}^{0.98\pm0.1} \Delta W_{\rm ELM}^{0.52\pm0.16} R_{\rm geo}^{1\pm0.4} \quad (3)$$

which results for DTT to be $\epsilon_{\parallel}^{\rm peak,DTT} = 2.10\,\mathrm{MJ\,m^{-2}}$ (figure 12).

Finally, the time scales of the ELM heat load is approximated by a triangular waveform with a decay time $\tau_{\rm decay} = 2\tau_{\rm ELM}$ in line with the free-streaming-particle models [16] (figure 13). The rise time $\tau_{\rm ELM}$ is well correlated with the time for the ion transport from the pedestal to the divertor $\tau_{\parallel} = 2\pi R q_{95}(1 + (3/2)^{0.5}\nu^*)/C_{s,\rm ped}$ where $C_{s,\rm ped} \approx \sqrt{kT_e/m_i}$ is the ion sound speed.

The results for DTT are $\tau_{\parallel,\rm DTT} = 250\,\mu$s and hence $\tau_{\rm ELM,DTT} = 591\,\mu$s.

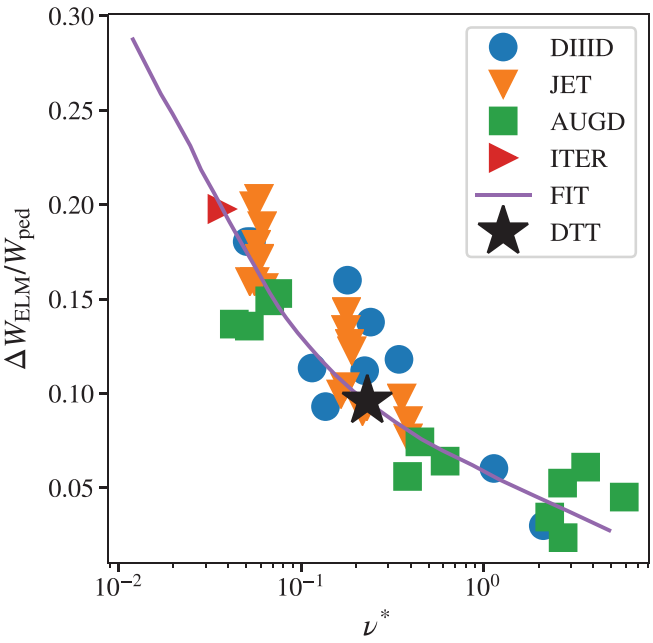

Figure 11. Multi-machine scaling of the relative energy loss during type-I ELMs.

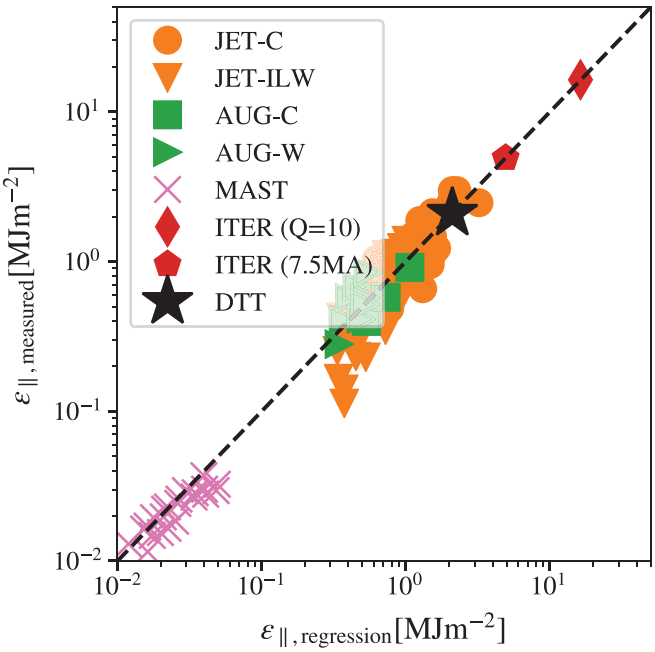

Figure 12. Multi-machine scaling of the maximum energy fluence during type-I ELMs [15].

The ELM power deposition can be calculated in time using the free streaming model [57] as follows [58]:

$$q_{\parallel,\rm FS}(t) = \Gamma_{\parallel,\rm FS}(t) T_e^{\rm ped} \left[\left(\frac{\tau}{t}\right)^2 + 1 \right]$$

where $q_{\parallel,\rm FS}$ and

$$\Gamma_{\parallel,\rm FS}(t) = \frac{2 n_e^{\rm ped} c_s^{\rm ped}}{L_{\parallel}/L_{\rm ELM}} \left(\frac{\tau}{t}\right)^2 \exp\left[-\left(\frac{\tau}{t}\right)^2 \right]$$

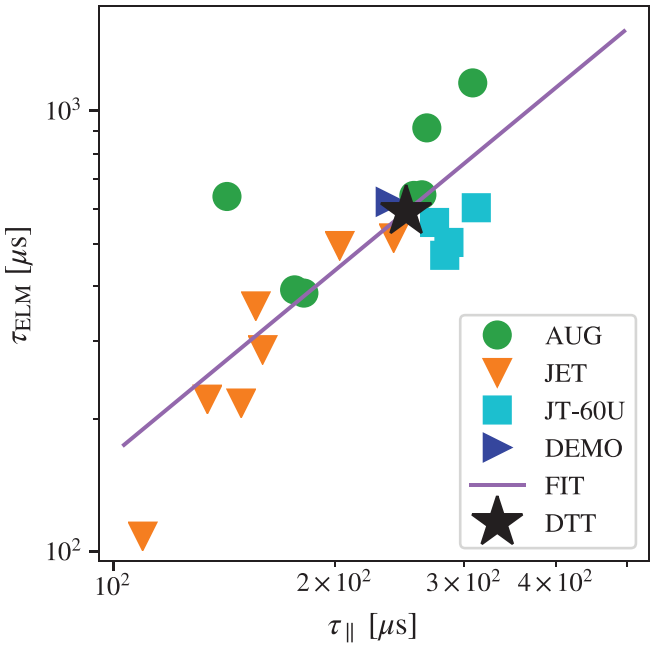

Figure 13. ELM-rise time τ_{ELM} as a function of time for the ion transport from the pedestal to the divertor $\tau_{\parallel}$.

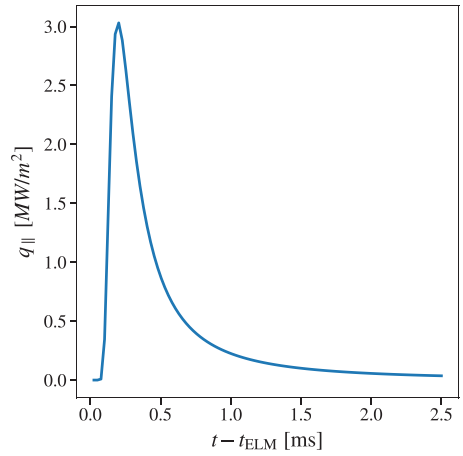

Figure 14. Type-I ELM evolution of the parallel heat flux in DTT.

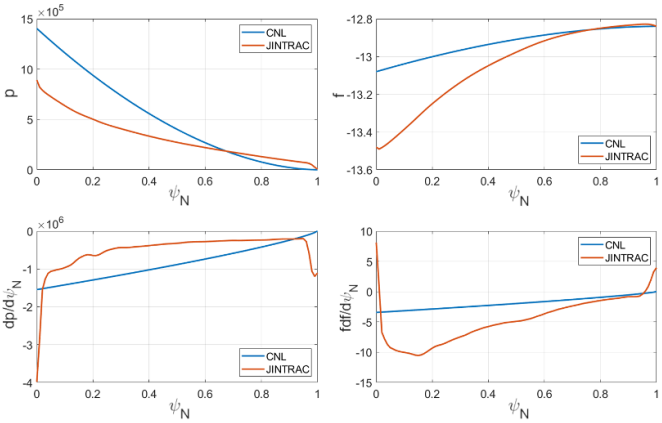

Figure 15. Comparison between CREATE-NL (CNL) and JINTRAC radial profiles of the pressure p, the f function, the pressure gradient $\mathrm{d}p/\mathrm{d}\psi_N$, and $f\mathrm{d}f/\mathrm{d}\psi_N$ for the E1 scenario during the flat-top phase. Bellshape plasma profiles are used as input in the CREATE-NL run. JINTRAC profiles refer to the QLK case with spread ECRH deposition.

are the parallel heat flux and the parallel ion flux at the divertor target surface location respectively. The resulting evolution of the parallel heat flux in DTT can be seen in figure 14.

More modelling work will be needed to assess the possible ELM frequency, since simple scalings such as reported in [17] are known to largely underestimate the ELM frequency in present devices.

As a final remark, since the density values at the separatrix are quite high ($n_e^{sep} \approx 0.8 \times 10^{20}\,\mathrm{m}^{-3}$), we could suspect the DTT E1 scenario to be in a type-II or small ELM regime [59]. Thus, a more detailed analysis on ELM stability and their inclusion in the integrated modelling work are envisaged for the future, but beyond the goal of this paper.

2.2.4. EM configuration consistency. To ensure the reliability of our modelling predictions, a key aspect is to guarantee the consistency between the electromagnetic configuration and plasma profiles calculated by transport models. Thus, a validation work of the coupling between the CREATE-NL and JINTRAC has been carried out for the SN flat-top configuration in the E1 scenario.

CREATE-NL is a 2D Finite Element Method code able to solve numerically Grad–Shafranov equation under the axisymmetric hypothesis. CREATE-NL is able to work both with 'bell-shaped' plasma current profiles [60] and with generic profiles for what concerns poloidal current function f and plasma pressure p.

The plasma boundary, as mentioned above, and the product between the major radius R_0 and the vacuum toroidal field value B_0 at the plasma centre provided by CREATE-NL calculations are used as settings for the integrated core simulations. In turn, the CREATE-NL runs require plasma profiles as input. Particularly, the starting reference DTT E1 SN plasma equilibria supplied by CREATE-NL were obtained assuming hypothetical bell-shape plasma profiles. Clearly, the integrated modelling work treated in the previous sections led to quite different profiles, as pointed out by the comparison figure 15. Therefore, an external feedback from CREATE-NL was essential to verify the configuration feasibility with the computed transport profiles.

A recalculation of the currents in the central solenoid (CS) and poloidal field (PF) coils required to achieve the desired plasma shape and the flat-top plasma boundary flux with the profiles determined by JINTRAC has been performed. Particularly, this consistency check between the control coil system capabilities and JINTRAC plasma profiles has been carried out for three simulations of the E1 scenario: the TGLF case with argon and central ECRH shown in figure 2, the QLK case with argon and central ECRH shown in figure 2 and in figure 7, and the QLK case with argon and spread ECRH shown in figure 7.

In all these cases, the same magnetic-separatrix shape with the JINTRAC plasma profiles has been recovered with good

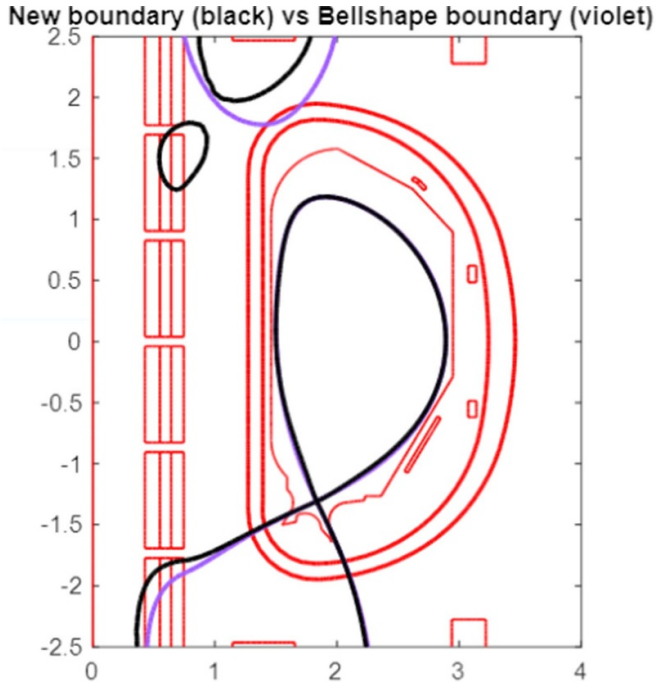

Figure 16. Comparison of the plasma boundary between the starting reference equilibrium calculated by CREATE-NL assuming bellshape plasma profiles (in violet) and the equilibrium recalculated by CREATE-NL in order to obtain the desired magnetic-separatrix shape assuming the JINTRAC plasma profiles (in black).

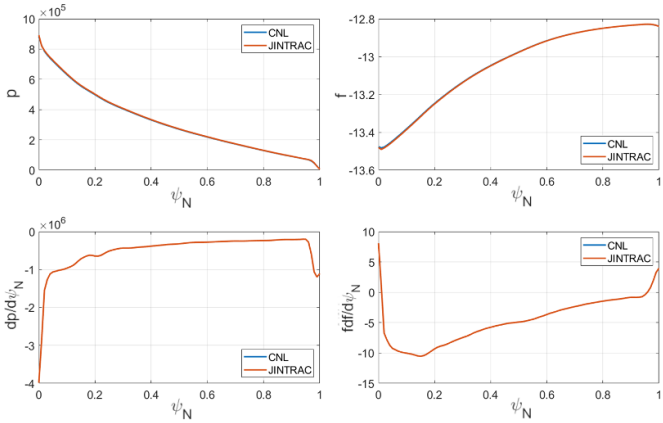

Figure 17. Comparison between JINTRAC radial profiles of the pressure p, the f function, the pressure gradient $\mathrm{d}p/\mathrm{d}\psi_\mathrm{N}$, and $f\mathrm{d}f/\mathrm{d}\psi_\mathrm{N}$ for the E1 scenario during the flat-top phase and CREATE-NL (CNL) profiles achieved with recalculated coil currents. JINTRAC profiles refer to the QLK case with spread ECRH deposition.

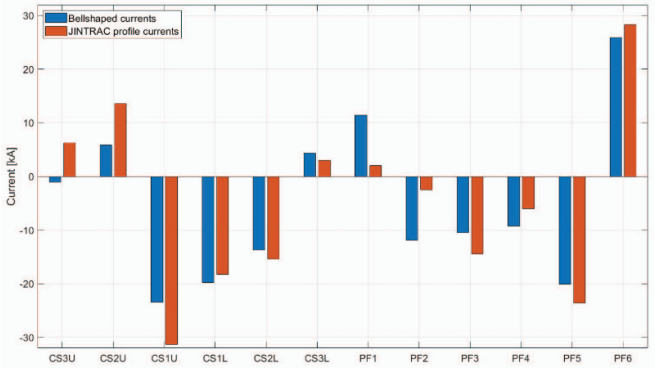

(a) JINTRAC run: TGLF case with Ar and central ECRH.

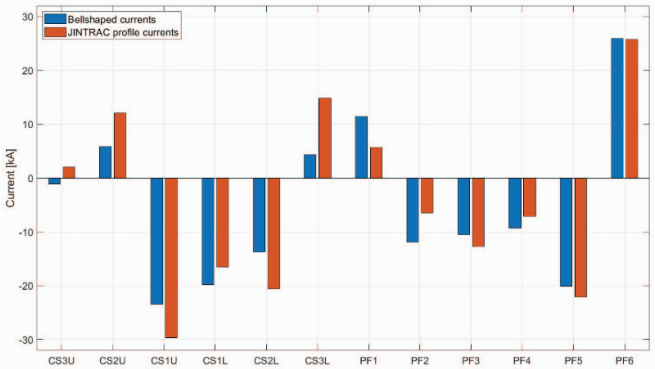

(b) JINTRAC run: QLK case with Ar and central ECRH.

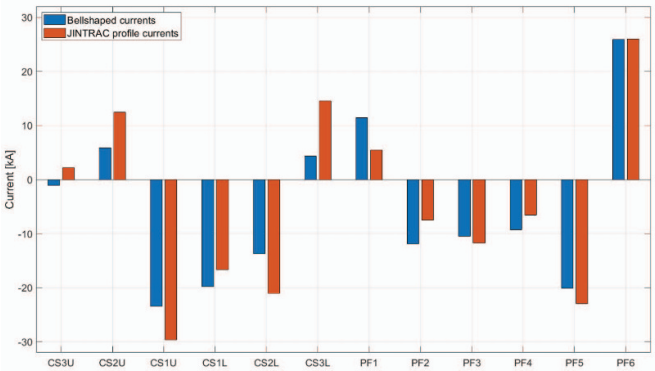

(c) JINTRAC run: QLK case with Ar and spread ECRH.

Figure 18. Comparison of the CS/PF currents between the starting reference equilibrium calculated by CREATE-NL assuming bellshape plasma profiles (in blue) and the equilibrium recalculated by CREATE-NL in order to obtain the desired plasma shape assuming the JINTRAC plasma profiles (in red), for three different JINTRAC runs.

agreement, as displayed in figures 16 for an example case. Moreover, the validation of the output profiles coming from this new iteration in CREATE-NL with the JINTRAC inputs against the JINTRAC profiles has been also done to guarantee the goodness of the procedure, as reported in figure 17 for an example case.

For every plasma profile set, significant variations of both the CS and PF coil currents are needed, as shown in figure 18. Nevertheless, even though these current changes are remarkable, they lie in a feasible range. Therefore, the plasma profiles calculated by transport models for the E1 scenario are compatible with the control coil system capabilities.

2.3. The C1 scenario

The C1 scenario works with full vacuum toroidal magnetic field $B_\mathrm{tor} = 5.85\,\mathrm{T}$, but with plasma reduced current $|I_\mathrm{pl}| = 4.0\,\mathrm{MA}$ compared to 5.5 MA for scenario E1.

Table 3. Comparison between SOL and core modelling main results for the C1 scenario.

	SOL modelling	Core modelling TGLF
Seeding impurity	Ne	Ne
$Z_{\rm eff}^{\rm ped}$	1.5–3.3	1.3
$Z_{\rm eff}^{\rm sep}$	2.3–4.0	2.6
$n_e^{\rm ped}$ (10^{20} m^{-3})	1.3–1.4	1.4
$C_{\rm seed.imp.}^{\rm ped}$ (10^{-2})	0.4–3.8	0.25
$C_{\rm W}^{\rm ped}$ (10^{-5})	—	6.0
$P_{\rm rad}$ (MW)	2.8–4.0	9.9
$[0.85 < \rho_{\rm tor} < 1.0]$		

In the C1 scenario, the auxiliary heating includes:

- 16 gyrotrons to provide a total ECRH power to the plasma of about 14.4 MW with beams in O-mode;
- 1 module with 2 RF antennas to provide a total ICRH power to the plasma of about 3.0 MW.

The ICRH heating profiles have been calculated by PION with the general settings described before, while a prescribed ECRH power deposition equal to the corresponding profile foreseen in [7] has been included.

The C1 pedestal has been calculated by a specific Europed modelling using in input temperatures at the separatrix of $T_e^{\rm sep} = T_i^{\rm sep} = 100$ eV, a pedestal top density of $n_e^{\rm ped} = 1.4 \times 10^{20}$ m^{-3}, a value of $\beta_{\rm pol} = 0.65$, a relative shift of $(T_e^{\rm pos} - n_e^{\rm pos}) = 0.006\psi_N$ in order to have $n_e^{\rm sep} \approx 0.45 \times 10^{20}$ m^{-3}, neon as impurity, and an effective charge of $Z_{\rm eff}$, obtaining a temperature of 2.3 keV at the pedestal top ($\rho_{\rm tor} = 0.89$).

In the C1 scenario core simulation, performed using the TGLF SAT2 model only, neon as seeding impurity and tungsten have been modelled, setting $Z_{\rm eff} = 1.4$ and $n_{\rm W}/n_{\rm Ne} = 0.03$ as initial conditions.

All these settings make the core modelling predictions compatible with radiation and impurity content values in SOL simulations convergent to a detached state. In table 3, the main modelling settings and results of SOL and core modelling of the C1 scenario are listed.

The C1 scenario, such as the full power one, has been found to be ITG dominant at all radii. Figure 19 shows the radial profiles of the electron temperature, ion temperature, electron density, safety factor, impurity densities, effective charge, and radiation achieved in this TGLF simulation of the C1 scenario. Figures 20(a) and (b) show respectively the radial profiles of power densities and total powers in the C1 scenario.

Although the ECRH power deposition is quite central, the ratio T_e/T_i and the density peaking are much lower than those of the TGLF case with neon and central ECRH deposition in the E1 scenario. It was expected due to the reduced ECRH power and to the lack of the NBI particle source. The Greenwald density fraction $\bar{n}_e/n_{\rm Gr} \approx 0.52$ (still well within safety margins) is similar to values of the E1 scenario, since the n_e profile flatness offsets the effect of using the same pedestal top density of the E1 case at a reduced plasma current.

The total neutron rate is about 1.7×10^{16} neutrons s^{-1} in the C1 scenario.

For the C1 scenario, the energy confinement time and the H-factor (with $P = P_{\rm sep}$) resulted respectively $\tau_E \approx 1.3$ s and $H_{98} \sim 1.6$.

2.4. The A1 scenario

The DTT first experimental plasma is the A1 scenario and will operate at half magnetic field $B_{\rm tor} = 3$ T and at reduced current $|I_{\rm pl}| = 2.0$ MA.

The auxiliary heating is provided only by a cluster of gyrotrons, coupling to the plasma about 7.2 MW of ECRH power in second harmonic X-mode (resulting above the L-H transition power, according to both the ITPA 2008 L-H threshold scaling [61] and the ITPA 2018 L-H threshold scaling for metallic wall devices [62, 63]). In the JINTRAC runs, the ECRH beams have been modelled by the GRAY code.

In relation to the EC launcher positioning of [46], the toroidal angles have been set in the following ranges: $+45.0^\circ$ for UP beams, $(-6.0^\circ) - (-0.5^\circ)$ for EQT beams, and $(-13.0^\circ) - (-5.0^\circ)$ for EQB beams. The poloidal angles have been set in the following ranges: $+22.5^\circ$ for UP beams, $+25^\circ$ for EQT beams, and $(+21.5^\circ) - (+25.0^\circ)$ for EQB beams. With these angle settings, the ECRH power density is deposited in the inner half of the plasma, precisely in the region $0.03 \leqslant \rho_{\rm tor} \leqslant 0.47$.

For the A1 scenario, nitrogen (N, $A \approx 14$, $Z = 7$) has been selected as suitable seeding impurity. Nitrogen and tungsten densities have been calculated by SANCO during the JINTRAC runs, setting $Z_{\rm eff} = 2.5$ and $n_{\rm W}/n_{\rm N} = 0.001$ as initial conditions.

To obtain the pedestal pressure for the A1 scenario, proper Europed simulations with the EPED model have been performed. Temperatures at the separatrix of $T_e^{\rm sep} = T_i^{\rm sep} = 100$ eV, a value of $\beta_{\rm pol} = 0.25$, a pedestal top density of $n_e^{\rm ped} = 0.50 \times 10^{20}$ m^{-3}, a relative shift of $(T_e^{\rm pos} - n_e^{\rm pos}) = 0.020\psi_N$ in order to obtain an electron density at the separatrix of $n_e^{\rm sep} \approx 0.34 \times 10^{20}$ m^{-3}, and an effective charge of $Z_{\rm eff} = 3.5$ have been set as inputs of the reference A1 pedestal run, predicting pedestal top temperatures of about 1.2 keV. The pedestal top density has been chosen to have a Greenwald fraction of about 0.47. With these settings, the electron density stays cautiously far from the second harmonic ECRH cut-off ($n_e = 1.79 \times 10^{20}$ m^{-3}).

The A1 scenario core modelling has been carried out using TGLF SAT2 as turbulent transport model and solving the transport equations up to the pedestal top ($\rho_{\rm tor} = 0.92$).

All these settings make the core modelling predictions compatible with the power exhaust requirements in terms of radiation and impurity content to operate in fully detached state. In table 4, the main modelling settings and results of SOL and core modelling of the DTT first plasma are listed. Notwithstanding some inevitable differences between core and SOL modelling values, a good compatibility is reached also for the A1 scenario.

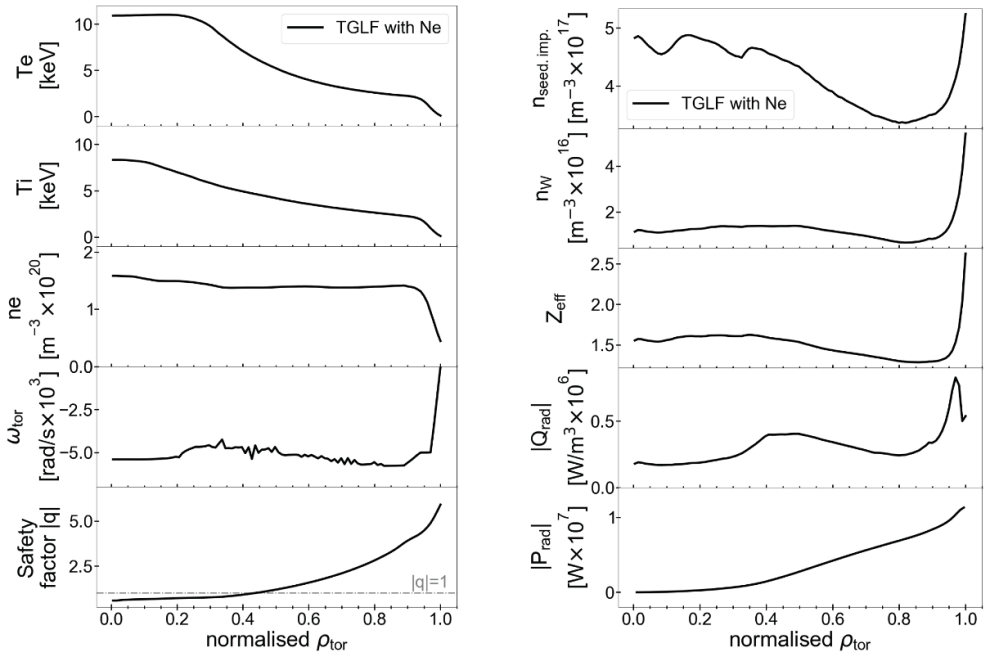

(a) (b)

Figure 19. Radial profiles for the C1 scenario flat-top phase (a) of the electron and ion temperatures, electron density, toroidal rotation, and safety factor absolute value and (b) of the seeding impurity and tungsten densities, effective charge, radiative power density, and radiative power.

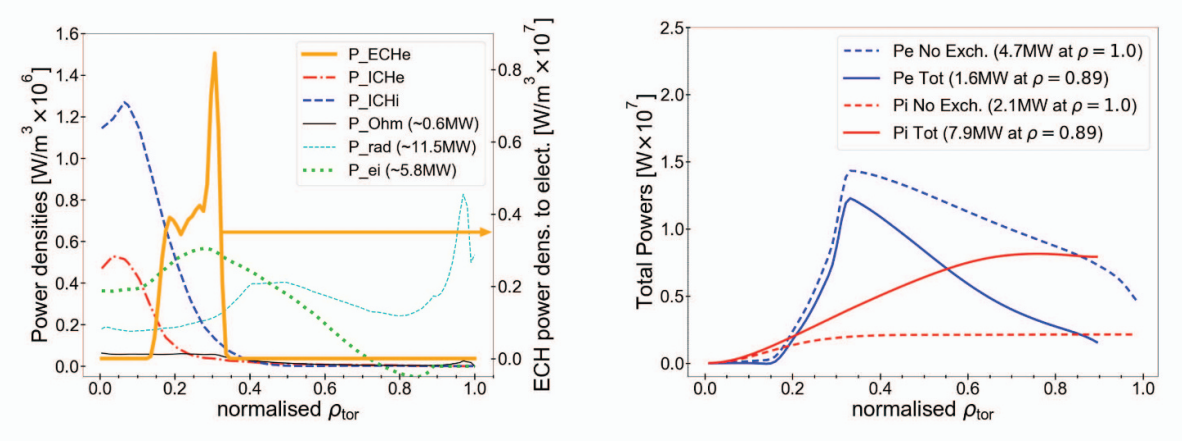

(a) Power densities. (b) Volume integrated powers.

Figure 20. (a) Radial profiles for the C1 scenario of power densities: ECRH power deposited to electrons $P_{\mathrm{ECRH}e}$, ICRH power deposited to electrons $P_{\mathrm{ICRH}e}$, ICRH power deposited to ions $P_{\mathrm{ICRH}i}$, Ohmic power P_{Ohm}, radiative power P_{rad}, and thermal exchange power between electrons and ions P_{ei}. (b) Radial profiles for the C1 scenario of electron and ion total powers including or not including the thermal exchange power between species.

The A1 scenario is dominated by TEMs within $\rho_{\mathrm{tor}} = 0.6$, while returns to be ITG dominant outside ($\rho_{\mathrm{tor}} > 0.6$). The radial profiles of electron temperature T_e, ion temperature T_i, electron density n_e, and safety factor $|q|$, nitrogen density $n_{\mathrm{seed.imp.}}$, tungsten density n_{W}, effective charge Z_{eff}, radiative power density Q_{rad}, and deposited ECRH power density $Q_{\mathrm{ECRH}e}$ of the A1 scenario are shown in figure 21.

We notice that T_i is much lower than T_e inside $\rho_{\mathrm{tor}} \sim 0.7$ (with $T_{e_0} \approx 8.8\,\mathrm{keV}$ and $T_{i_0} \approx 3.3\,\mathrm{keV}$), due to having low density ($n_{e_0} \approx 0.81 \times 10^{20}\,\mathrm{m}^{-3}$) and only electron heating. The impurities do not accumulate in the centre significantly as shown in figure 21(b) and the total radiative power is $P_{\mathrm{rad}} \approx 1.5\,\mathrm{MW}$.

Figure 22 shows the radial profiles of the total electron and ion powers, with and without thermal coupling.

For the A1 scenario, a neutron rate of about 2×10^{14} neutrons s^{-1} is assessed. The energy confinement time and the H-factor (with $P = P_{\mathrm{sep}}$) are respectively $\tau_E \approx 0.36\,\mathrm{s}$ and $H_{98} \approx 1.2$ in the A1 scenario of DTT.

Table 4. Comparison between SOL and core modelling main results for the A1 scenario.

	SOL modelling	Core modelling TGLF
Seeding impurity	N	N
$Z_{\text{eff}}^{\text{ped}}$	3.3	2.4
$Z_{\text{eff}}^{\text{sep}}$	2.9–4.1	3.7
n_e^{ped} $(10^{20}\ \text{m}^{-3})$	6.9–7.8	5.0
$C_{\text{seed.imp.}}^{\text{ped}}$ (10^{-2})	8.0–10.0	3.2
$C_{\text{W}}^{\text{ped}}$ (10^{-5})	—	3.3
P_{rad} (MW) $[0.85 < \rho_{\text{tor}} < 1.0]$	0.65–0.68	1.2

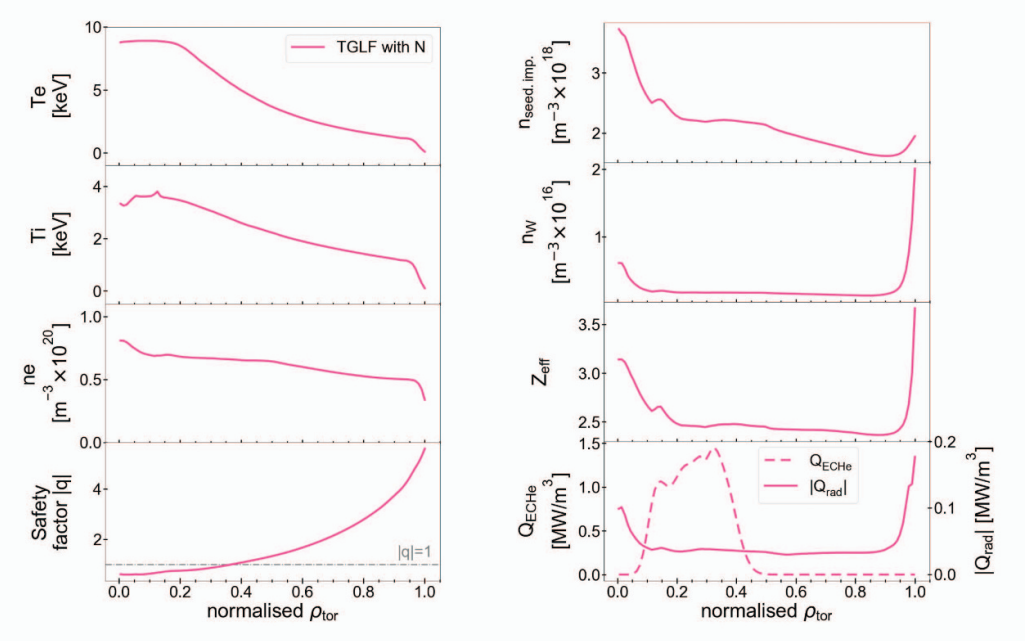

(a) (b)

Figure 21. Radial profiles of the A1 scenario referred to a TGLF run with nitrogen. (a) Profiles of electron and ion temperatures, electron density, and safety factor. (b) Profiles of impurity densities, effective charge, radiative power, and ECRH power density.

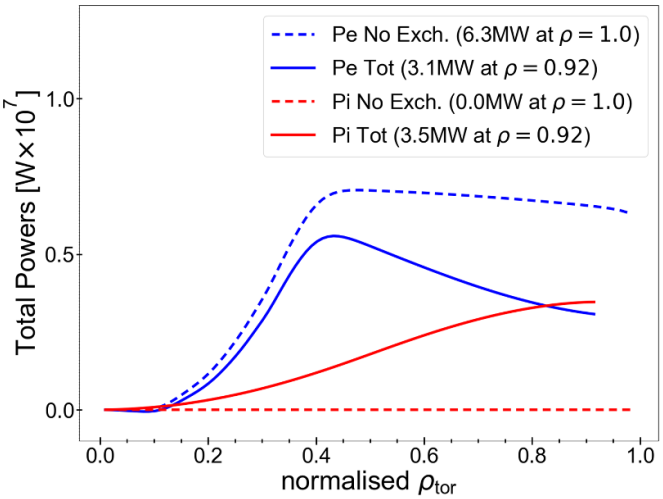

Figure 22. Radial profiles for the A1 scenario of electron and ion total powers including or not including the thermal exchange power between species.

Table 5. Main parameters of different DTT scenarios.

Scenario	β_{pol}	β_{tor}	β_N	H_{98} ($P = P_{sep}$)	τ_E (s)	W_{pl} (MJ)	$\lvert q_{95}\rvert$
A1	∼0.6	∼0.013	∼1.3	∼1.2	∼0.36	∼2.3	∼4
C1	∼0.5	∼0.013	∼1.3	∼1.6	∼1.3	∼8.8	∼4
E1	0.35–0.5	0.016–0.022	1.2–1.6	0.7–1.1	0.3–0.5	9–16	2.7–2.9

3. Conclusions

The main baseline scenarios of the DTT facility during the flat-top phase were extensively studied for the new device configuration, including the machine enlargement and the additional heating system upgrades. In this first principle multi-channel integrated modelling work, theory based QL transport models (QLK [26, 27] and TGLF SAT2 [24, 25]) were used to ensure the highest fidelity currently achievable. Moreover, a long iterative work of key parameter adjustment led to a good agreement between core and SOL simulations, improving the reliability of our modelling predictions. In addition, the consistency of the plasma profiles calculated by transport models with the electromagnetic configuration achievable by the control coil system were also checked for the E1 scenario. A summary table 5 indicates the main results of the reference DTT scenarios.

In this updated modelling of the E1 scenario with the new DTT configuration, in order to fulfil the SOL requirements, a density value at the separatrix of about $n_e^{sep} \approx 0.8 \times 10^{20}\,\mathrm{m}^{-3}$ was set. This is much larger than typical values of plasma discharges in existing tokamaks and than values in previous DTT simulations [7]. This choice entailed a change in the relative shift of density and temperature pedestals $(T_e^{pos} - n_e^{pos})$ and a very high density gradient in the pedestal, harder to be handled. The present choice for the full power scenario of a Greenwald fraction of about $\bar{n}_e/n_{Gr} \approx 0.5$, implies $T_e \gg T_i$ over almost the whole plasma radius. Raising the Greenwald fraction will be possible, leading to a better balance between T_e and T_i, but mostly via a T_e reduction, because high ion stiffness binds the T_i profile tightly to the ITG critical gradient. Such high stiffness is also consistent with the observation that the E1 scenario has very similar T_i profiles to the C1 scenario, in spite of roughly double additional power. Possible ways of reducing ion stiffness through fast ions have been reported in literature [64–67], but including these effects in integrated simulations requires an upgrade of existing QL transport models. Although the electron density is moderately peaked in the E1 scenario, the tungsten does not accumulate in the plasma centre. In the C1 and A1 scenarios a flatter density profile has been found, as expected due to the lack of the NBI. For the first time the sawteeth were included in DTT E1 scenario simulations and a wide analysis for optimising EC launching angles with the aim of improving the E1 safety factor profile was done. The Porcelli and Kadomtsev models have been used respectively to trigger the sawteeth and to predict the relaxed temperature, density, and $|q|$ profiles after a crash. The ST frequency with a complete reconnection is $f_{ST} \approx 1.4$ Hz, while with an incomplete reconnection with a fraction of $f_{rec} = 0.8$ is $f_{ST} \approx 1.7$ Hz. Furthermore, first estimations of the DTT ELMs in the E1 scenario were performed through suitable scalings. The calculated loss of plasma energy due to one ELM is about 10% of the pedestal energy in the reference E1 scenario.

Data availability statement

The data that support the findings of this study are available upon reasonable request from the authors.

Acknowledgments

This work is carried out in the framework of the DTT design activity. The authors are very grateful to all the colleagues involved in the DTT project for their precious contribution. We thank G Tardini for providing help for the simulations with ASTRA code. We thank G M Staebler and J Citrin for providing advice on the use of the TGLF and QLK models respectively. This work was part-funded by the RCUK Energy Programme (Grant No. EP/T012250/1). The first author has worked under a PhD grant financed by ENEA.

ORCID iDs

I Casiraghi https://orcid.org/0000-0002-1719-6682
P Mantica https://orcid.org/0000-0001-5939-5244
L Aucone https://orcid.org/0000-0003-3949-678X
B Baiocchi https://orcid.org/0000-0002-1483-3113
L Balbinot https://orcid.org/0000-0002-7467-533X
M Cavedon https://orcid.org/0000-0002-0013-9753
L Frassinetti https://orcid.org/0000-0002-9546-4494
P Agostinetti https://orcid.org/0000-0003-2103-7630
L Figini https://orcid.org/0000-0002-0034-4028
P Vincenzi https://orcid.org/0000-0002-5156-4354

References

[1] Electricity F 2012 A roadmap to the realisation of fusion energy (available at: www.euro-fusion.org/fileadmin/user_upload/Archive/wp-content/uploads/2013/01/JG12.356-web.pdf)
[2] EUROfusion 2018 European research roadmap to the realisation of fusion energy (available at: www.euro-fusion.org/fileadmin/user_upload/EUROfusion/Documents/2018_Research_roadmap_long_version_01.pdf)
[3] ITER Project (available at: www.iter.org/)
[4] DEMO project (available at: www.euro-fusion.org/programme/demo/)
[5] R Martone, R Albanese, F Crisanti, P Martin and A Pizzuto (eds) 2019 *Divertor Tokamak Test Facility: Interim Design Report (Green Book)* (available at: www.dtt-dms.enea.it/share/s/avvglhVQT2aSkSgV9vuEtw)

[6] DTT project (available at: www.dtt-project.it)
[7] Casiraghi I *et al* 2021 *Nucl. Fusion* **61** 116068
[8] Balbinot L Rubino G and Innocente P 2021 *Nucl. Mater. Energy* **27** 100952
[9] Bufferand H *et al* 2013 *J. Nucl. Mater.* **438** S445–8
[10] Bufferand H *et al* 2015 *Nucl. Fusion* **55** 053025
[11] DTT Plant Integration Document (DTT PID), version 3.2 (last update 07 July 2022). Currently this document is not public, but information and clarifications can be requested to (available at: info@dtt-project.it)
[12] Innocente P, Ambrosino R, Brezinsek S, Calabró G, Castaldo A, Crisanti F, Dose G, Neu R and Roccella S 2022 *Nucl. Mater. Energy* **33** 101276
[13] Porcelli F, Boucher D and Rosenbluth M N 1996 *Plasma Phys. Control. Fusion* **38** 2163–86
[14] Loarte A *et al* 2007 *Phys. Scr.* **128** 222–8
[15] Eich T *et al* 2017 *Nucl. Mater. Energy* **12** 84–90
[16] Eich T *et al* 2009 *J. Nucl. Mater.* **390–391** 760–3
[17] Loarte A *et al* 2003 *Plasma Phys. Control. Fusion* **45** 1549–69
[18] Balbinot L *et al* 2022 *Nucl. Mater. Energy* **34** 101350
[19] Romanelli M 2014 *Plasma and Fus. Res.* **9** 3403023
[20] Cenacchi G and Taroni A 1988 Report *ENEA-RT-TIB* 88-5
[21] Pereverzev G V and Yushmanov P N 2002 ASTRA automated system for transport analysis in a tokamak *IPP Report 5/98* (Max-Planck-Institut für Plasmaphysik)
[22] Fable E *et al* 2013 *Plasma Phys. Control. Fusion* **55** 124028
[23] Houlberg W A Shaing K C, Hirshman S P and Zarnstorff M C 1997 *Phys. Plasmas* **4** 3230–42
[24] Staebler G M, Candy J, Howard N T and Holland C 2016 *Phys. Plasmas* **23** 062518
[25] Staebler G M, Candy J, Belli E A, Kinsey J E, Bonanomi N and Patel B 2021 *Plasma Phys. Control. Fusion* **63** 015013
[26] Bourdelle C, Citrin J, Baiocchi B, Casati A, Cottier P, Garbet X and Imbeaux F 2016 *Plasma Phys. Control. Fusion* **58** 014036
[27] Stephens C D, Garbet X, Citrin J, Bourdelle C, van de Plassche K L and Jenko F 2021 *J. Plasma Phys.* **87** 905870409
[28] Pereverzev G V and Corrigan G 2008 *Comput. Phys. Commun.* **179** 579–85
[29] Saarelma S, Challis C D, Garzotti L, Frassinetti L, Maggi C F, Romanelli M and Stokes C 2018 *Plasma Phys. Control. Fusion* **60** 014042
[30] Snyder P B, Groebner R J, Hughes J W, Osborne T H, Beurskens M, Leonard A W, Wilson H R and Xu X Q 2011 *Nucl. Fusion* **51** 103016
[31] Dunne M G *et al* 2017 *Plasma Phys. Control. Fusion* **59** 014017
[32] Frassinetti L *et al* 2019 *Nucl. Fusion* **59** 076038
[33] Frassinetti L *et al* 2021 *Nucl. Fusion* **61** 126054
[34] Frassinetti L *et al* 2021 *Nucl. Fusion* **61** 016001
[35] Taroni L 1994 *21st EPS Conf. Contr. Fus. Plas. Phys. (Montpellier)* vol 102
[36] Huber A *et al* 2020 *Phys. Scr.* **2020** 014055
[37] Castaldo A, Albanese R, Ambrosino R and Crisanti F 2022 *Energies* **15** 1702
[38] Albanese R, Ambrosino R and Mattei M 2015 *Fusion Eng. Des.* **96–97** 664–7
[39] Peeters A, Angioni C, Camenen Y, Casson F J, Hornsby W A, Snodin A P and Strintzi D 2009 *Phys. Plasmas* **16** 062311
[40] Peeters A G *et al* 2011 *Nucl. Fusion* **51** 094027
[41] Farina D 2007 *Fusion Sci. Technol.* **52** 154–60
[42] Vincenzi P *et al* 2023 Interaction of high–energy neutral beams with Divertor Tokamak Test plasma *Fus. Eng. Design* **189** 113436
[43] Challis C D Cordey J G, Hamnén H, Stubberfield P M, Christiansen J P, Lazzaro E, Muir D G, Stork D and Thompson E 1989 *Nucl. Fusion* **29** 563
[44] Agostinetti P, Bolzonella T, Gobbin M, Sonato P, Spizzo G, Vallar M and Vincenzi P 2019 *Fusion Eng. Des.* **146** 441–6
[45] Eriksson L-G, Hellsten T and Willen U 1993 *Nucl. Fusion* **33** 1037
[46] Garavaglia S *et al* 2021 *Fusion Eng. Des.* **168** 112678
[47] Görler T *et al* 2011 *J. Comput. Phys.* **230** 7053–71
[48] GENE code (available at: www.genecode.org/)
[49] Garofalo A M *et al* 2014 *Fusion Eng. Des.* **89** 876–81
[50] Baiocchi B *et al* 2023 Predictive studies of deuterium fuelling strategies in the Divertor Tokamak Test facility *Plasma Phys. Control. Fusion* submitted
[51] Kadomtsev B B 1975 *Fiz. Plazmy* **1** 710
[52] Kadomtsev B B 1976 *Sov. J. Plasma Phys.* **2** 389
[53] O'Rourke J 1991 *Plasma Phys. Control. Fusion* **33** 289
[54] Levinton F M, Batha S H, Yamada M and Zarnstorff M C 1993 *Phys. Fluids* B **5** 2554
[55] Sauter O *et al* 2002 *Phys. Rev. Lett.* **88** 105001
[56] Igitkhanov Y and Bazylev B 2014 *IEEE Trans. Plasma Sci.* **42** 2284–90
[57] Fundamenski W, Pitts R A and (JET EFDA contributors) 2006 *Plasma Phys. Control. Fusion* **48** 109
[58] Abrams T *et al* 2018 *Nucl. Mater. Energy* **17** 164–73
[59] Harrer G F *et al* 2018 *Nucl. Fusion* **58** 112001
[60] Luxon J L and Brown B B 1982 *Nucl. Fusion* **22** 813
[61] Martin Y R *et al* 2008 *J. Phys.: Conf. Ser.* **123** 012033
[62] Delabie E *et al* 2014 Overview and interpretation of L-H threshold experiments on JET with the ITER–like wall *25th IAEA Fusion Energy Conf. (St Petersburg, Russia 13–18 October 2014)* pp 5–24
[63] Delabie E *et al* 2018 Status of TC–26: L–H/H–L scaling in the presence of metallic walls *ITPA Transport & Confinement Meeting Fall*
[64] Citrin J, Jenko F, Mantica P, Told D, Bourdelle C, Garcia J, Haverkort J W, Hogeweij G M D, Johnson T and Pueschel M J 2013 *Phys. Rev. Lett.* **111** 155001
[65] Di Siena A, Görler T, Doerk H, Poli E and Bilato R 2018 *Nucl. Fusion* **58** 054002
[66] Di Siena A, Görler T, Poli E, Navarro A B, Biancalani A and Jenko F 2019 *Nucl. Fusion* **59** 124001
[67] Di Siena A *et al* 2021 *Phys. Rev. Lett.* **127** 025002